Theoretical and Applied Mechanics Letters 6 (2016) 81–96

Contents lists available at ScienceDirect

Theoretical and Applied Mechanics Letters

journal homepage: www.elsevier.com/locate/taml

Letter

Elastic properties of chiral, anti-chiral, and hierarchical honeycombs: A simple energy-based approach

Davood Mousanezhad [a], Babak Haghpanah [a], Ranajay Ghosh [a], Abdel Magid Hamouda [b], Hamid Nayeb-Hashemi [a], Ashkan Vaziri [a,*]

[a] Department of Mechanical and Industrial Engineering, Northeastern University, Boston, MA 02115, USA
[b] Mechanical and Industrial Engineering Department, Qatar University, Doha, Qatar

HIGHLIGHTS

- Effects of chirality and hierarchy on elastic response of honeycombs are studied.
- Closed-form relations are derived for elastic moduli and validated using finite element method (FEM).
- Chirality always decreases the stiffness and Poisson's ratio.
- Hierarchical refinement increases the stiffness in hexagon based honeycombs.
- Anti-tetra-chiral structure shows anisotropy, auxeticity, and low shear stiffness.

ARTICLE INFO

Article history:
Received 12 January 2016
Received in revised form
26 February 2016
Accepted 29 February 2016
Available online 11 March 2016
*This article belongs to the Solid Mechanics

Keywords:
Chiral
Hierarchical
Honeycomb
Metamaterial
Auxetic

ABSTRACT

The effects of two geometric refinement strategies widespread in natural structures, chirality and self-similar hierarchy, on the in-plane elastic response of two-dimensional honeycombs were studied systematically. Simple closed-form expressions were derived for the elastic moduli of several chiral, anti-chiral, and hierarchical honeycombs with hexagon and square based networks. Finite element analysis was employed to validate the analytical estimates of the elastic moduli. The results were also compared with the numerical and experimental data available in the literature. We found that introducing a hierarchical refinement increases the Young's modulus of hexagon based honeycombs while decreases their shear modulus. For square based honeycombs, hierarchy increases the shear modulus while decreasing their Young's modulus. Introducing chirality was shown to always decrease the Young's modulus and Poisson's ratio of the structure. However, chirality remains the only route to auxeticity. In particular, we found that anti-tetra-chiral structures were capable of simultaneously exhibiting anisotropy, auxeticity, and remarkably low shear modulus as the magnitude of the chirality of the unit cell increases.

Among the most readily observed topological features in natural structures are chirality [1–5], hierarchy [6–13], and hierarchy of chirality [14,15]. Their abundance in nature can be contrasted with traditional man-made constructions, which often rely on multiple materials selection but relatively simpler micro-geometrical constitution. In recent years, following these topological cues, synthetic metamaterials with non-traditional properties such as negative stiffness [16–18], auxeticity [19–22], and negative thermal expansion [23–25] have been proposed. These characteristics make mechanical metamaterials suitable for applications such as novel prostheses [26], fasteners [27], piezo-composites with optimal performance [28], dome-shaped panels [29,30], and high structural integrity foams [31].

Among this general class of metamaterials, periodic chiral lattices such as the ones shown in Fig. 1 have been shown to possess relatively compliant behavior because of their bending dominated response, while exhibiting considerable multi-axial expansion/contraction under uniaxial loads due to auxeticity [32,33]. These features make them optimal candidates for flexible design applications such as micro-electro-mechanical-systems (MEMS) [19,34,35], aircraft morphing structures [36–43], and as analogues of spokes in non-pneumatic tires [44,45]. In addition, chiral honeycombs have been experimentally and numerically shown to possess Poisson's ratios in the range of $-1 < \nu < 0$. For instance, Alderson et al. [46] studied the in-plane elastic

* Corresponding author.
E-mail address: vaziri@coe.neu.edu (A. Vaziri).

http://dx.doi.org/10.1016/j.taml.2016.02.004

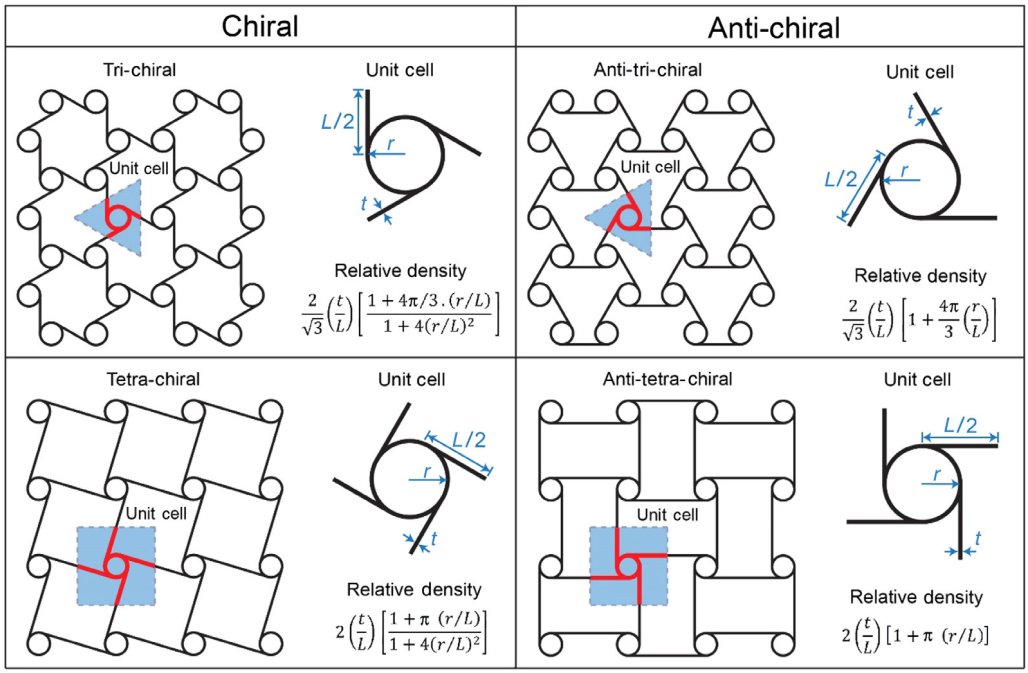

Fig. 1. Schematic of the structure and the unit cell, and the expression of relative density for the chiral and anti-chiral honeycombs studied.

constants of chiral and anti-chiral honeycombs using finite element (FE) analysis and experiments. Continuing further, Alderson et al. [47] investigated the in-plane linear elastic response and out-of-plane bending of tri- and anti-tri-chiral honeycombs and their re-entrant counterparts using FE analysis and experiments. Nonetheless, closed-form expressions of elastic moduli for most of these structures are still unavailable. Among several two-dimensional (2D) chiral lattices proposed in the literature, only the elastic properties of hexa- and tetra-chiral lattices have been investigated analytically, using micro-polar and second-gradient continuum theories [32,48–51]. These approaches are far more complex than the simple yet robust method used here for analytical study of chiral unit cells, which often require special boundary conditions at the unit cell level due to underlying rotational symmetry of the structure.

Another class of bio-inspired materials used increasingly to broaden the achievable range of mechanical response is the hierarchically structured material systems. Extreme values of material properties such as specific stiffness [11,52–54], toughness [55–58], strength [11,53,59,60], buckling strength [61], negative or complex Poisson's ratio [62–65], and phononic band gaps [66] have been reported in hierarchical architectures across multiple length scales. Through a series of studies on the strength of different fractal-like structures under various loads, Farr and co-workers [59,67–70] suggested that the volume of the material used for a stable structure can be reduced by an order of 3–4 under mild loads using hierarchical designs of third and fourth generation. However, the advantage of hierarchical design in these structures diminishes as the magnitude of applied loading increases. Ajdari et al. [52] showed that a type of self-similar hierarchical honeycomb is capable of attaining specific Young's modulus as much as 2 and 3.5 times that of a regular hexagonal lattice through first and second orders of hierarchy, respectively. In a more inclusive study that considered enhancements in multiple parameters, Haghpanah et al. [71] showed that a wide range of specific stiffness and strength can be tailored by introducing higher orders of hierarchy in a hexagonal lattice. However, none of these earlier studies specifically focused on investigating the geometry of hierarchy as a controlling variable of mechanical properties of honeycombs. Moreover, there is no systematic comparison between hierarchy and chirality in the literature, which can be useful in design and selection of structures for different loading conditions.

In light of this discussion, it becomes clear that further investigations on the behavior of these classes of metamaterials are well justified. Particularly, obtaining closed-form analytical expressions for the elastic constants in terms of geometric and material parameters would constitute an important step towards evaluating and designing these materials. Furthermore, it would also foster a better understanding of the role of chirality and hierarchy in influencing the mechanical response of these materials. To this end, in the current paper, we carry out a systematic theoretical and computational study of the effects of these two natural geometrical organizations — chirality and hierarchy — on the in-plane elastic response of 2D honeycombs. In order to directly compare the effects of chirality versus hierarchy, we limit the results to first order of hierarchy for the hierarchical structures presented here. An energy-based method is used to obtain the unit cell deformation by satisfying both the periodic boundary conditions and symmetry requirements for the unit cell. Two specific types of regular tessellation with square and hexagonal cells are altered to endow them with chirality and hierarchy. For achieving chirality, the square based unit cell is altered to yield two different types of chiral architectures — tetra-chiral and anti-tetra-chiral — whereas the hexagonal unit cell alteration results in tri-chiral and anti-tri-chiral structures (illustrated in Fig. 1). In contrast to chiral microstructures, hierarchy is achieved by both conserving the rotational and reflective symmetries of the lattice. This is done by replacing the nodes in a periodic network of cells with the original cells albeit of smaller size as shown in Fig. 2. Thus, the introduction of hierarchy into the square unit cell results in hierarchical square and hierarchical diamond honeycombs (illustrated in Fig. 2). In order to proceed with our calculations, the representative volume element (RVE) is used as the fundamental unit of analysis. In a periodic lattice material, the RVE (i.e., unit cell) is identified as the smallest volume which with associated tractions and displacements, tessellates the space to represent the whole lattice structure under loading [60]. We choose the shaded triangular and square areas bounded by dashed lines in Figs. 1 and 2 as

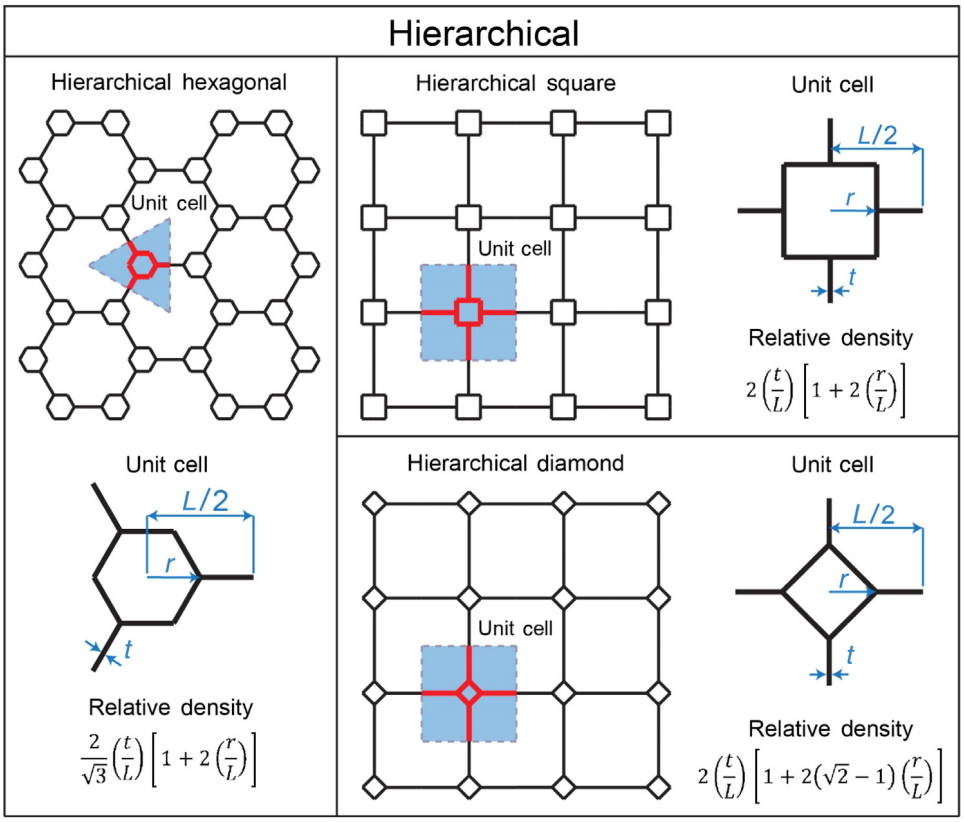

Fig. 2. Schematic of the structure and the unit cell, and the expression of relative density for the hierarchical honeycombs studied.

the structural unit cells of the structures under study. This implies that under any in-plane loading, we can tile the 2D space, solely by translating, and/or reflecting, and/or rotating (by 180°) the unit cells and their corresponding tractions and displacements, to represent the infinitely extended 2D structures.

We first describe and derive the elastic moduli (i.e., Young's and shear moduli, and Poisson's ratio) of chiral and anti-chiral structures. This is followed by a section devoted to deriving the elastic constants for the hierarchical structures. The results are then compared in a unified template to highlight the effects brought about by these geometrical variants. The paper ends with conclusions.

Chiral and anti-chiral structures studied in this paper have an array of cylinders (nodes) connected by tangential ligaments (ribs) as shown in Fig. 1. Depending on the number of ligaments tangential to each cylinder, two types of chiral lattices are introduced: tri- and tetra-chiral structures which are respectively composed of 3 and 4 tangential ligaments for each cylinder. Similarly, anti-chiral lattices are generated if any two adjacent cylinders share the same side of the common tangential ligament. Thus, in addition, two anti-chiral lattices are introduced which are called anti-tri- and anti-tetra-chiral structures (see Fig. 1).

The structural organization of the chiral and anti-chiral honeycombs can be defined by the ratio, r/L, where r is the radius of the cylinders and L is the length of the ligaments as described in Fig. 1. This figure also represents the dimensionless relative density (i.e., area fraction) of the structures in terms of r/L and t/L, where t is the thickness of the cell walls. For the special case, where $r = 0$, the normalized relative density of the hexagon (tri-chiral and anti-tri-chiral) and square (tetra-chiral and anti-tetra-chiral) based chiral and anti-chiral honeycombs respectively reduce to that of regular hexagonal $[2/\sqrt{3}\cdot(t/L)]$ and square $(2t/L)$ honeycombs.

Here, we derive closed-form expressions for elastic properties of chiral and anti-chiral honeycombs made of an isotropic linear elastic material with Young's modulus, E_s. In contrast to the previous studies [32,33,48–51], we employ a simple energy-based procedure (Castigliano's second theorem [72]) to obtain analytical estimates for elastic properties of the structures under study. A three-fold symmetry seen within the tri- and anti-tri-chiral lattices (see Fig. 1) assures the macroscopic isotropy of their in-plane elastic properties [73]. Thus, for complete characterization of these structures, they each need only two elastic constants to be determined (i.e., Young's modulus and Poisson's ratio) (shear modulus is obtained as a function of the other two elastic constants, analogous to isotropic materials). In principle, these elastic constants can be determined by any kind of in-plane loading. However, in this study, without loss of generality we chose uniaxial loading to obtain the Young's modulus and Poisson's ratio. In contrast, the four-fold symmetry of tetra- and anti-tetra-chiral honeycombs causes the structures to exhibit macroscopic anisotropy in their in-plane elastic behavior. Therefore, all the components of their stiffness (or compliance) tensor have to be determined in order to fully identify their elastic behavior. For tetra- and anti-tetra-chiral lattices, we first chose a coordinate system such that the x and y axes were aligned to the lines connecting the center of adjacent cylinders together. This symmetry requires one Young's modulus, one Poisson's ratio, one shear modulus, and possibly two more coefficients called "the coefficients of mutual influence of the first kind" [74] (they characterize the normal strains caused by shear stresses).

To this end, for each of the anisotropic honeycombs (tetra- and anti-tetra-chiral structures), we first impose a uniaxial loading in the x-direction (i.e., horizontal direction in Fig. 1) to obtain the structure's Young's modulus, E_x, and Poisson's ratio, ν_{xy}. Note that the sub-index x, is used to emphasize that the elastic constants are obtained as a result of a loading in the x-direction and they are not valid for any other directions (except for y-direction (i.e., vertical direction in Fig. 1), due to symmetry) of in-plane loading since the structures do not have an isotropic in-plane behavior. Furthermore

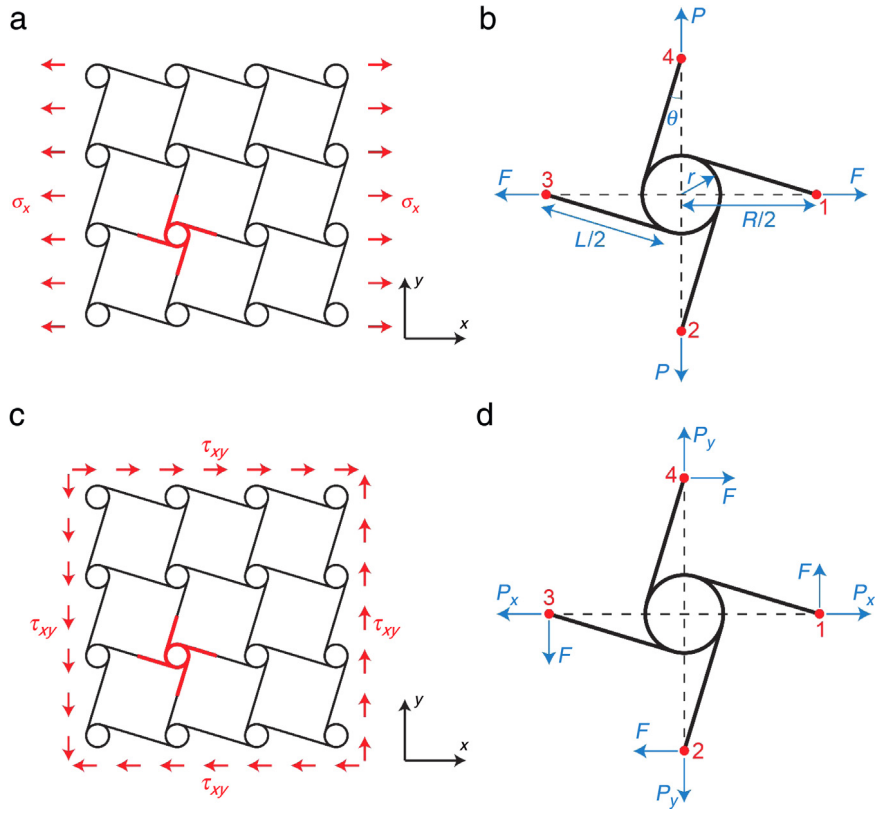

Fig. 3. (a) Schematic of a tetra-chiral honeycomb under x-direction uniaxial loading. (b) Free body diagram of the structural unit cell under uniaxial loading. (c) Schematic of a tetra-chiral honeycomb under x-y shearing load. (d) Free body diagram of the structural unit cell under shearing load.

due to this anisotropy, in order to obtain the shear modulus, G_{xy}, and the coefficients of mutual influence of the first kind, we apply a separate shearing load to these structures. It is noteworthy that since these structures are stretching dominated in both the x- and y-directions, we must include the stretching terms in addition to bending terms in computing the strain energy of the unit cells. In contrast, for bending dominated structures, we only include the bending terms of strain energy. In our theoretical calculations, the central cylinders appearing in the unit cells are regarded as perfectly rigid elements. Also the rotation of ligaments and cylinders is neglected due to small deformation assumption. These assumptions significantly reduce the complexity of the problem yielding closed-form expressions for elastic moduli while staying reasonably accurate for most of the geometries considered in this study.

In the next paragraphs, we will derive closed-form expressions for the elastic moduli of tetra-chiral structures as a demonstration of our proposed method. The detailed derivations for other chiral and anti-chiral structures are presented in Appendices.

A schematic of a tetra-chiral structure, which is based on an underlying square network, undergoing a uniaxial far-field stress in the x-direction, σ_x is shown in Fig. 3(a). The free body diagram (FBD) of the corresponding unit cell is shown in Fig. 3(b). The unit cell contains a cylinder (node) which is assumed to be rigid and four half ligaments. Due to the 180° rotational symmetry of the structure and the components of the microscopic stresses, all four external cut points of the unit cell (i.e., points 1 through 4 in Fig. 3(b)) must be moment-free under an arbitrary macroscopic stress state. Also, since the only far-field stress acting on the structure is along the x-direction, all the external cut points must be force-less except points 1 and 2 which carry a pair of forces with opposite directions along the x-direction due to σ_x. Therefore, unknown forces and moments acting on the unit cell's external cut points can be summarized as shown in Fig. 3(b), where F can be determined as a function of applying stress as, $F = \sigma_x R$, where R is the center to center distance between any two adjacent cylinders. Moreover, to be able to determine the structure's Poisson's ratio, a pair of virtual forces, P is also added on points 2 and 4 of the unit cell. The strain energy of the unit cell is given as:

$$U = 2\frac{(F\cos\theta)^2 L/2}{2E_s A} + 2\frac{(P\cos\theta)^2 L/2}{2E_s A} + 2\int_0^{L/2}\frac{(xF\sin\theta)^2}{2E_s I}\mathrm{d}x + 2\int_0^{L/2}\frac{(xP\sin\theta)^2}{2E_s I}\mathrm{d}x, \tag{1}$$

where E_s (as mentioned earlier) is the Young's modulus of the cell wall material, A is the cross sectional area of cell walls (i.e., for a rectangular cross section with unit depth, $A = t$), I is the second moment of area of the wall's cross section (cell walls are assumed to have a rectangular cross section with uniform thickness, t, and unit depth, i.e., $I = t^3/12$), and $\theta = \tan^{-1}(2r/L)$ is the angle between each ligament and the line connecting the centers of two adjacent cylinders as shown in Fig. 3(b). Next, $\partial U/\partial F|_{P=0}$ gives the total displacement of point 1 with respect to point 3 in the x-direction as, $\delta_x = \frac{FL}{E_s A}\cos^2\theta + \frac{FL^3}{12E_s I}\sin^2\theta$. From this, we can now calculate the structure's average strain in the x-direction as, $\epsilon_x = \delta_x/R$. The Young's modulus of the structure normalized by material's Young's modulus is then defined as the ratio of the average stress, σ_x and the average strain, ϵ_x and obtained as:

$$E_x/E_s = \frac{t/L}{\cos^2\theta + \sin^2\theta/(t/L)^2}. \tag{2}$$

On the other hand, $\partial U/\partial P|_{P=0}$ gives the total displacement of points 2 and 4 in the direction of virtual forces as $\delta_y = 0$. Therefore, $\epsilon_y = \delta_y/R = 0$ and this will result in $\nu_{xy} = 0$.

In the next step, we seek to determine the structure's shear modulus with respect to the x–y coordinate system. To this end,

we consider a tetra-chiral structure undergoing a uniform far-field shear stress, τ_{xy}, as shown in Fig. 3(c). FBD of a representative unit cell is also shown in Fig. 3(d). The 180° rotational symmetry of the structure implies unit cell's all four external cut points (i.e., points 1 through 4 in Fig. 3(d)) to be moment free. Furthermore, each of these external cut points must be free of any normal forces (in the direction passing through the cut point and center of the cylinder), because there is no macroscopic normal stress acting on the structure in those directions. Thus, there are only four equal shearing forces acting on the unit cell's external cut points, F, which can be obtained as a function of applying stress as, $F = \tau_{xy}R$. We also apply two pairs of virtual forces, P_x, and P_y to the unit cell to be able to find the average strains in the x- and y-directions due to the applying shear stress. Therefore, based on the loadings on the unit cell shown in Fig. 3(d), the strain energy is given as the following:

$$\begin{aligned} U = {} & 2\frac{(F\sin\theta - P_x\cos\theta)^2 L/2}{2E_sA} + 2\frac{\left(F\sin\theta + P_y\cos\theta\right)^2 L/2}{2E_sA} \\ & + 2\int_0^{L/2} \frac{[(F\cos\theta + P_x\sin\theta)\,x]^2}{2E_sI}\mathrm{d}x \\ & + 2\int_0^{L/2} \frac{\left[\left(F\cos\theta - P_y\sin\theta\right)x\right]^2}{2E_sI}\mathrm{d}x. \end{aligned} \tag{3}$$

Next, $(\partial U/\partial F|_{P_x=P_y=0})/R$ gives the total change of angle between two straight lines initially parallel to the x- and y-axes which is the direct measure of the shear strain, γ_{xy}. Then, the shear modulus of the structure normalized with respect to the Young's modulus of cell wall material, is defined as the ratio of the average shear stress, τ_{xy} to the average shear strain, γ_{xy} and given as the following:

$$G_{xy}/E_s = \frac{0.5\,(t/L)^3}{\cos^2\theta + (t/L)^2\sin^2\theta}. \tag{4}$$

Note that as θ goes to zero, the structure transforms into a regular square honeycomb. Upon substituting $\theta = 0$ into the closed-form expressions for E_x and G_{xy}, we obtain $E_x/E_s = t/L$, and $G_{xy}/E_s = 0.5\,(t/L)^3$, which are the Young's and shear moduli of a regular square honeycomb, respectively [75]. For all values of θ, Poisson's ratio is equal to that of square honeycomb, $\nu_{xy} = 0$.

From the above calculations, the structure's 2D compliance tensor can be formed as the following:

$$\boldsymbol{S} = \begin{bmatrix} S_{11} & S_{12} & S_{13} \\ S_{12} & S_{22} & S_{23} \\ S_{13} & S_{23} & S_{33} \end{bmatrix}, \tag{5}$$

where $S_{11} = S_{22} = 1/E_x$, $S_{12} = -\nu_{xy}/E_x$, and $S_{33} = 1/G_{xy}$. Then, to completely determine all components of 2D compliance tensor of this structure, we still need to obtain S_{13} and S_{23}, which can respectively be given by calculating the average normal strains of the structure in the x- and y-directions due to the shearing load. $(\partial U/\partial P_x|_{P_x=P_y=0})/R$ and $(\partial U/\partial P_y\big|_{P_x=P_y=0})/R$ give the average normal strains in the x- and y-directions (ϵ_x and ϵ_y), respectively. Then, S_{13} and S_{23} are respectively defined as the ratio of the resulting normal strains in the x- and y-directions to the applying shear stress and given as the following:

$$\begin{aligned} S_{13} &= \frac{\epsilon_x}{\tau_{xy}} = +\left[(L/t)^3 - (L/t)\right]\sin\theta\cos\theta/E_s, \\ S_{23} &= \frac{\epsilon_y}{\tau_{xy}} = -\left[(L/t)^3 - (L/t)\right]\sin\theta\cos\theta/E_s. \end{aligned} \tag{6}$$

Next, in order to find the orientation of principal coordinate system (i.e., directions in which S_{13} and S_{23} are both equal to zero which implies that no normal strains can be produced under shear stress) we rotate the x–y–z coordinate system with respect to the z-axis by an angle α (positive when counter-clockwise). The compliance tensor in the new system, $\bar{\boldsymbol{S}}$ is determined using the compliance transformation rule [74], $\bar{\boldsymbol{S}} = \boldsymbol{T}\boldsymbol{S}\boldsymbol{T}^{\mathrm{T}}$, where $\boldsymbol{T}$ is the rotation tensor defined as:

$$\boldsymbol{T} = \begin{bmatrix} m^2 & n^2 & mn \\ n^2 & m^2 & -mn \\ -2mn & 2mn & (m^2 - n^2) \end{bmatrix}, \tag{7}$$

where $m = \cos\alpha$, and $n = \sin\alpha$. Performing this transformation, we will end up with $\bar{S}_{13} = -\bar{S}_{23} = \frac{1}{2E_s}(L/t)\left[(L/t)^2 - 1\right] \times \sin(2\theta + 4\alpha)$. Thus, $\bar{S}_{13} = -\bar{S}_{23} = 0$ gives the orientation of the principal axes as, $\alpha = k\pi/4 - \theta/2$, where k is an integer.

Similar procedure has been performed to obtain closed-form expressions of elastic moduli for tri-, anti-tri-, and anti-tetra-chiral structures and the details have been presented in Appendices.

In this section, we investigate the linear elastic properties of hierarchical structures. To this end, we select two representative samples, hierarchical square and hierarchical diamond, which are respectively generated by replacing the vertices of a regular square honeycomb by smaller squares and diamonds (see Fig. 2). The wall thickness of the structures is simultaneously reduced to maintain the overall density equal to that of regular square honeycomb.

Similar to chiral and anti-chiral honeycombs, the structural organization of hierarchical structures can be defined by the ratio, r/L, where r and L are defined for each structure in Fig. 2. This figure also represents the dimensionless relative density (i.e., area fraction) of the structures in terms of r/L and t/L. For the special case, where $r = 0$, the normalized relative density of the hexagon (hierarchical hexagonal honeycomb), and square (hierarchical square and hierarchical diamond) based hierarchical structures respectively reduce to that of regular hexagonal $[2/\sqrt{3}\cdot(t/L)]$, and square $(2t/L)$ honeycombs.

Note that among these three hierarchical structures shown in Fig. 2, Ajdari et al. [52] studied the in-plane elastic properties of hierarchical hexagonal honeycombs. Thus, in the current paper we focus on the other two structures and just report the results published by the authors for the sake of completeness.

Similar to the previous section, Castigliano's second theorem is used to derive closed-form relations for elastic properties of hierarchical structures made of an isotropic linear elastic material with Young's modulus, E_s. It should be noted that hierarchical square and diamond structures exhibit macroscopic anisotropy. Thus, in order to completely characterize their elastic behavior we need to obtain the Young's modulus, Poisson's ratio, and shear modulus along the principal directions. To this end, first a uniaxial loading in the x-direction is applied to each structure to determine the structure's Young's modulus, E_x and Poisson's ratio, ν_{xy} and then a shearing load is imposed to obtain the shear modulus, G_{xy}. Finally the orientation of principal coordinate systems is given for each structure. In contrast to chiral and anti-chiral lattices where we assumed the cylinders to be rigid, here we assume the entire structure including smaller squares and diamonds to have a linear elastic material property.

We will obtain closed-form expressions of the elastic moduli for hierarchical square structures as a demonstration of our proposed method. The details of the procedure for hierarchical diamond structures are presented in Appendices.

A schematic of a hierarchical square honeycomb under a uniaxial far-field stress in the x-direction, σ_x is shown in Fig. 4(a). A detailed FBD of the structural unit cell of this structure is shown in Fig. 4(b). It contains a smaller square and four half ligaments connecting the smaller squares together. Due to 180° rotational symmetry of the structure and components of microscopic stress, all external cut points of the unit cell (i.e., points 1 through 4 in

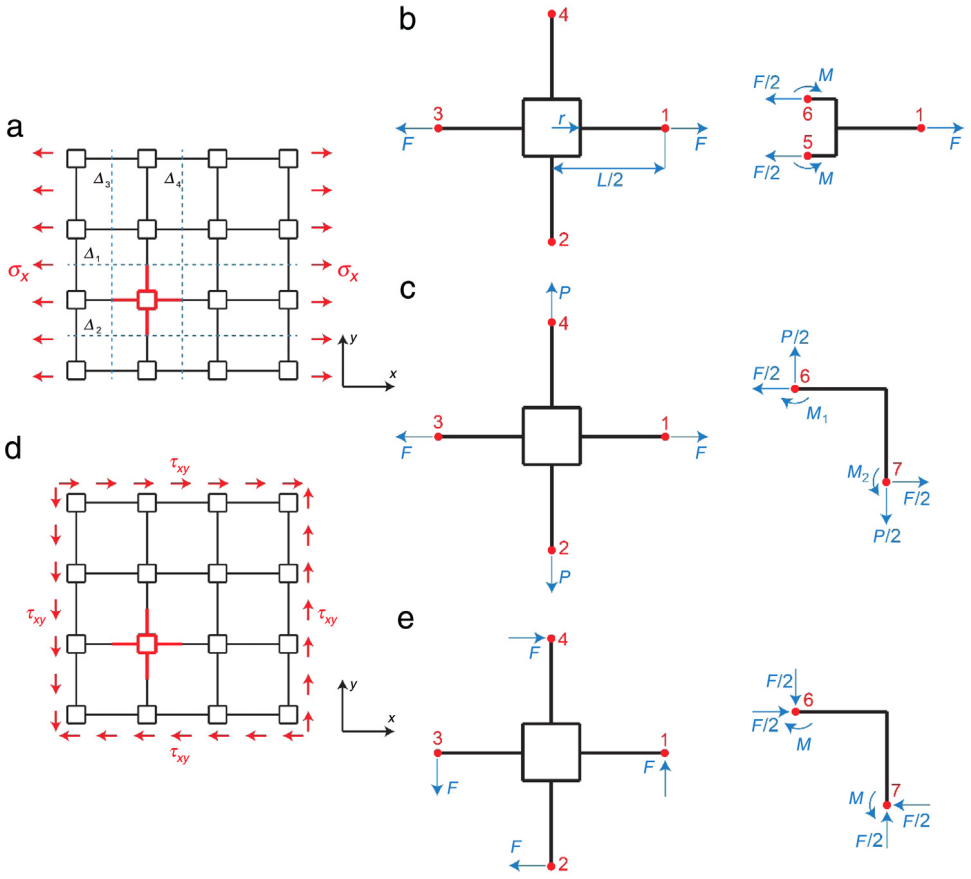

Fig. 4. (a) Schematic of a hierarchical square honeycomb under x-direction uniaxial loading. (b) and (c) Free body diagram of the structural unit cell under uniaxial loading, where P is a virtual force used for Poisson's ratio calculations. (d) Schematic of a hierarchical square honeycomb under x-y shearing load. (e) Free body diagram of the structural unit cell under shearing load.

Fig. 4(b)) must be moment free. Furthermore, by using a cut line Δ_1, we can see that since there is no macroscopic stress on the structure in the y-direction, the unit cell must be free of any forces in the y-direction at point 4. Similar arguments also hold true for point 2. Also note that the structure is symmetric with respect to all four cut lines shown in Fig. 4(a). This implies that the component of forces parallel to these cut lines at corresponding external cut point must be equal to zero. Thus, under the uniaxial stress on the structure, σ_x, each unit cell experiences the loading shown in Fig. 4(b), where F can be obtained as a function of applied stress as, $F = \sigma_x L$.

In order to determine the distribution of forces and moments at any cross section of the smaller square (needed for strain energy calculation in the next step), let us consider the right portion of the unit cell as illustrated in Fig. 4(b) (right). For equilibrium to be satisfied for forces in the x-direction, two equal forces, $F/2$ must be applied to points 5 and 6. Also, shear forces at these two points must be equal to zero due to the fact that no macroscopic stress is being applied to the structure in the y-direction. Moreover, symmetry of the structure requires that the rotation of point 5 (and similarly point 6) with respect to the z-axis be equal to zero. Using Castigliano's theorem, this condition is equivalent to the relation, $\partial U/\partial M = 0$, where U is the total strain energy of the portion of the unit cell shown in Fig. 4(b) and M is a yet unknown moment to be determined. This constraint will result in $M = rF/8$. Now, the unit cell's strain energy can be obtained as:

$$U = 2\frac{F^2\,(L/2-r)}{2E_sA} + 4\frac{(F/2)^2\,r}{2E_sA} + 4\frac{(rF/8)^2\,r}{2E_sI} + 4\int_0^r \frac{(rF/8 - xF/2)^2}{2E_sI}\mathrm{d}x. \tag{8}$$

Using above equation, the total displacement of point 1 with respect to point 3 in the x-direction can be calculated as, $\delta_x = \frac{\partial U}{\partial F} = \frac{F(L-r)}{E_sA} + \frac{10Fr^3}{48E_sI}$. Next, the structure's average strain in the x-direction is obtained by using the relation, $\epsilon_x = \delta_x/L$. The Young's modulus of the structure normalized by material's Young's modulus is then defined as the ratio of the average stress, σ_x and the average strain, ϵ_x and obtained as:

$$E_x/E_s = \frac{t/L}{1-(r/L)+2.5\,(r/L)^3\,/\,(t/L)^2}. \tag{9}$$

Next, in order to calculate the Poisson's ratio, let us consider a pair of virtual forces acting on the unit cell in the lateral direction, as shown in Fig. 4(c). One fourth of the smaller square of this unit cell is also shown in Fig. 4(c). Similar procedure as employed earlier is used to determine the unknown moments, M_1 and M_2, acting on points 6 and 7 as $M_1 = rF/8 - 3rP/8$ and $M_2 = rP/8 - 3rF/8$. Thus, the strain energy of the unit cell is given as:

$$U = 2\frac{F^2\,(L/2-r)}{2E_sA} + 2\frac{P^2\,(L/2-r)}{2E_sA} + 4\frac{(F/2)^2\,r}{2E_sA} + 4\frac{(P/2)^2\,r}{2E_sA} + 4\int_0^r \frac{(xF/2 + rP/8 - 3rF/8)^2}{2E_sI}\mathrm{d}x + 4\int_0^r \frac{(xP/2 + rF/8 - 3rP/8)^2}{2E_sI}\mathrm{d}x. \tag{10}$$

Now using Castigliano's second theorem on the strain energy calculated in Eq. (10) we obtain $\delta_y = \partial U/\partial P|_{P=0} = \frac{-Fr^3}{8E_sI}$. Using this equation, we obtain $\epsilon_y = \delta_y/L$ which is the structure's average

strain in the y-direction due to the uniaxial loading, σ_x. Poisson's ratio, ν_{xy} is then defined as the negative of the ratio of the average strain in the y-direction, ϵ_y to the average strain in the x-direction, ϵ_x and obtained as:

$$\nu_{xy} = \frac{0.6\,(r/L)^3}{(r/L)^3 - 0.4\,(t/L)^2\,(r/L) + 0.4\,(t/L)^2}. \tag{11}$$

Finally, to determine the shear modulus, as shown in Fig. 4(d), we apply a uniform far-field shear stress, τ_{xy} to the structure. A FBD of the unit cell of the structure is also shown in Fig. 4(e). The 180° rotational symmetry of the structure implies unit cell's all four external cut points (i.e., points 1 through 4 in Fig. 4(e)) to be moment free. Furthermore, each of these external cut points must be free of any normal forces (in the direction of the ligament), because there is no macroscopic normal stress acting on the structure in those directions. Thus, there are only four equal shearing forces acting on the unit cell's external cut points, F, which can be obtained as a function of applying stress as, $F = \tau_{xy}L$. Next, consider one fourth of the smaller square as shown in Fig. 7(e). Using the equilibrium equations, components of unknown forces and moment acting on the external cut points of this portion of the unit cell can be determined as functions of F, as shown in Fig. 4(e), where $M = (F/2)\cdot(L/2 - r)$. Hence, the strain energy of the unit cell can be written as:

$$U = 4\int_0^{L/2-r} \frac{(Fx)^2}{2E_sI}\mathrm{d}x + 8\frac{(F/2)^2\,r}{2E_sA} + 8\int_0^{r} \frac{[(F/2)\,(L/2 - r) - Fx/2]^2}{2E_sI}\mathrm{d}x. \tag{12}$$

Then, $(\partial U/\partial F)/L$ gives the total change of angle between two straight lines initially parallel to the x- and y-axes (i.e., the shear strain, γ_{xy}). Finally, shear modulus of the structure (G_{xy}, normalized with respect to the Young's modulus of cell walls material) is defined as the ratio of the average shear stress, τ_{xy} to the average shear strain, γ_{xy} and obtained as the following:

$$G_{xy}/E_s = \frac{0.5\,(t/L)^3}{1 - 3\,(r/L) - 6\,(r/L)^2 + 20\,(r/L)^3 + (t/L)^2\,(r/L)}. \tag{13}$$

Note that as r goes to zero, the structure transforms into a regular square honeycomb. Upon substituting $r = 0$ into Eqs. (9), (11) and (13), we obtain $E_x/E_s = t/L$, $\nu_{xy} = 0$, and $G_{xy}/E_s = 0.5\,(t/L)^3$, which are the Young's modulus, Poisson's ratio, and shear modulus of a regular square honeycomb, respectively. The principal directions for the 2D compliance tensor (S_{13} and S_{23} are both equal to zero for the current x–y–z coordinate system) of this structure can be calculated as, $\alpha = k\pi/4$, where k is an integer.

Similar procedure has been performed to obtain closed-form expressions of elastic moduli for hierarchical diamond structures and demonstrated in detail in Appendices.

In order to validate the theoretical expressions of elastic moduli, FE-based numerical models were developed to conduct simulations on the structures. We carry out FE analysis at the structural level instead of the unit cell level with 2D models of the structures constructed using the FE software ABAQUS 6.11-2 (SIMULIA, Providence, RI). The relative characteristic length of the samples with respect to the unit cells was sufficiently large enough to mitigate boundary effects on the inner unit cells. The models were meshed using in-plane 2-node linear beam elements allowing for shear deformation (i.e., B21 beam element in ABAQUS) and a mesh sensitivity analysis was carried out to guarantee that the results were not mesh-dependent. Static-general solver of ABAQUS was used to simulate the response of these structures under uniaxial compression and shearing loads. Cell walls were assumed to have a rectangular cross section with unit length

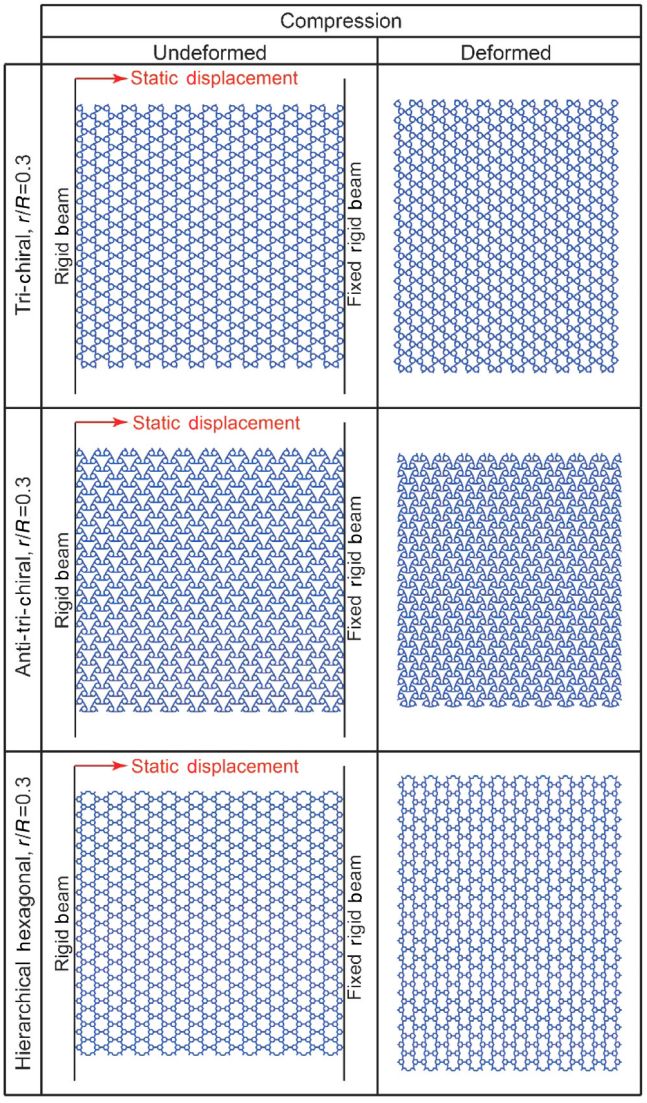

Fig. 5. Schematic diagrams of the FE models constructed in ABAQUS for simulating static uniaxial loads, as well as their corresponding exaggerated deformed configurations, for the structures with hexagon based grids with $r/R = 0.3$.

normal to the loading plane (i.e., normal to the x–y plane). R was taken to be equal to unity and the thickness (t) was adjusted to be consistent with the value of the relative density presented in Figs. 1 and 2. Linear elastic properties of aluminum were assumed for the cell wall material with $E_s = 70$ GPa and $\nu_s = 0.3$.

Figures 5 and 6 show the schematic diagrams of the FE models constructed in ABAQUS for simulating static uniaxial and shearing loads, as well as their corresponding exaggerated deformed configurations, for the structures with underlying hexagon and square based grids, respectively. In order to simulate the uniaxial loading, constant static displacement was assigned to the left nodes (see Figs. 5 and 6), while the horizontal displacement of the right nodes was constrained (i.e., set to zero). Then, to eliminate any boundary effects, periodic boundary conditions were imposed on the structures on the top- and bottom-side nodes [76]. Also note that the vertical displacement of an arbitrary node was constrained (i.e., set to zero) in order to prevent rigid body motion of the structure in that direction. To simulate the square based honeycombs under shearing loads, shear forces were applied to the boundary nodes, while the horizontal and vertical displacements of an arbitrary node were constrained (i.e., set to zero) to avoid rigid body motion, Fig. 6.

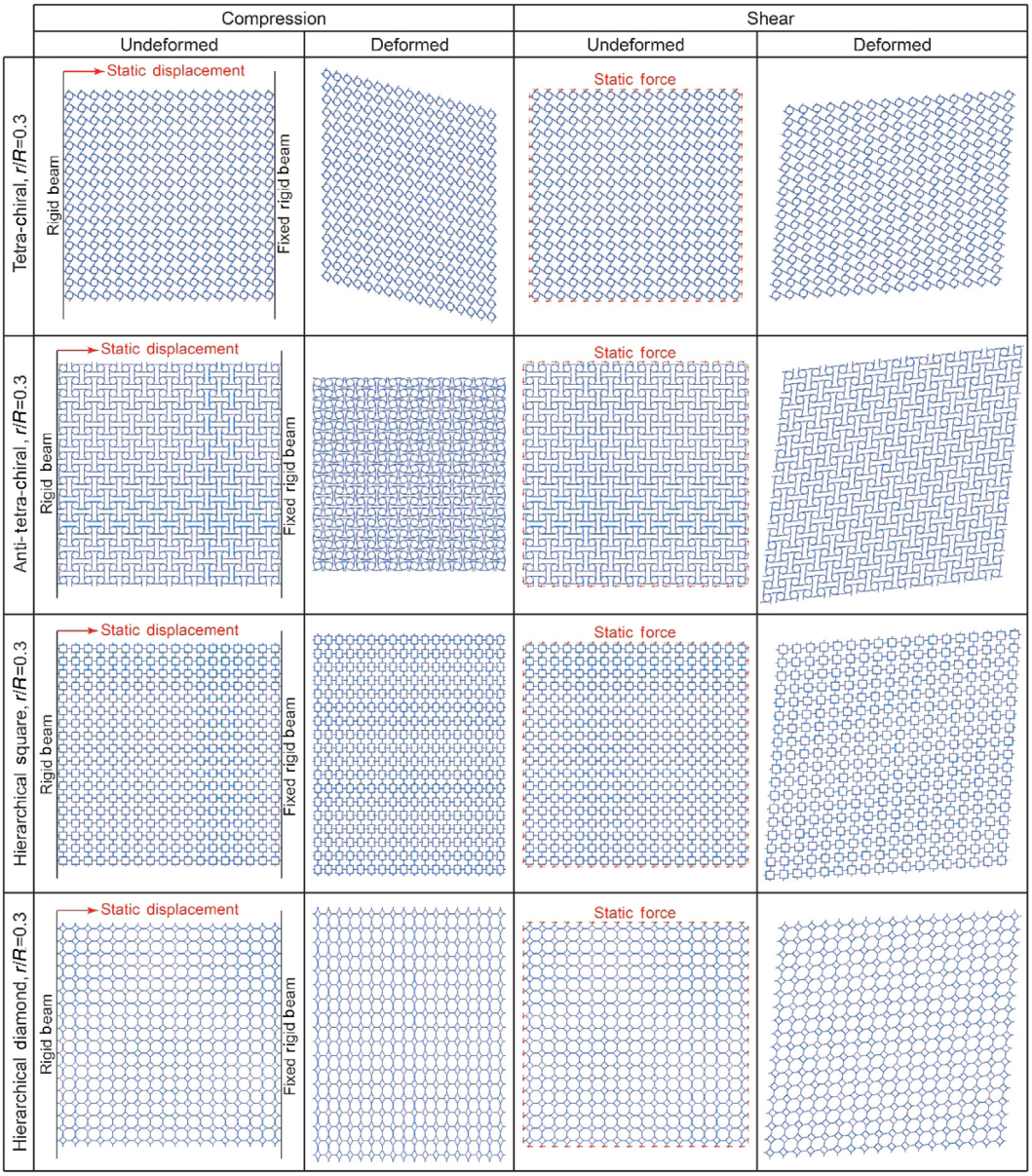

Fig. 6. Schematic diagrams of the FE models constructed in ABAQUS for simulating static uniaxial and shearing loads, as well as their corresponding exaggerated deformed configurations, for the structures with square based grids with $r/R = 0.3$.

The analytical expressions of effective Young's modulus (Young's modulus of the structure normalized by cell wall material's Young's modulus), Poisson's ratio, and effective shear modulus (shear modulus of the structure normalized by cell wall material's Young's modulus) for the meta-lattices studied are tabulated in Tables 1 and 2. In Table 1, the structures are characterized into two categories—hexagon and square based honeycombs. The structural unit cell, effective Young's modulus, and Poisson's ratio for each structure are reported in the next columns. For anisotropic structures (i.e., square based honeycombs), the effective shear modulus and material principal directions are reported in Table 2.

In Fig. 7, we plot the normalized Young's modulus (effective Young's modulus of the structure normalized by the effective Young's modulus of a regular hexagonal honeycomb with same relative density) (Fig. 7(a)) and the Poisson's ratio (Fig. 7(b)) of hexagon based chiral and hierarchical honeycombs varied via the r/R ratio which is a de-facto measure of the magnitude of alteration to the underlying structure. The solid lines represent the results from the analytical estimates of elastic moduli in Table 1 and markers denote the FE results. Note that Fig. 7(a) is a log–log plot. Clearly as $r/R \to 0$, the chiral and hierarchical structures reduce trivially to the regular hexagonal honeycomb. A good agreement is observed between the theoretical and FE results except for tri-chiral structure where the theory predicts higher stiffness and negative Poisson's ratio when $r/R > 0.2$. This discrepancy is resulted from the assumed rigid behavior for the cylindrical components in the chiral structures. When $r/R \to 0.5$ in the tri-chiral structure, the cylindrical components become the only source of compliance for the structure as straight beams vanish, and therefore the theoretical results diverge from the FE results. Among the hexagon based structures, hierarchical hexagonal honeycomb shows higher stiffness with respect to the other structures and the normalized Young's modulus achieves the maximum value of $\bar{E} \cong 2$ at $r/R \cong 0.32$ [52]. The plot of Poisson's ratio shown in Fig. 7(b) also shows a good agreement with the theoretical derivations presented earlier. Unlike the hierarchical structure, the chiral and anti-chiral structures are capable of showing auxetic behavior (i.e., negative Poisson's ratio) at higher r/R values. The anti-tri-chiral structure which

Table 1
Summary of the analytical relations for the effective Young's modulus and Poisson ratio of cellular lattices studied in this article. Asterisks (*) highlight anisotropic lattices. For these anisotropic lattices the analytical expressions for the effective shear modulus and material principal directions are given in Table 2.

	Name	Unit cell	Effective Young's modulus	Poisson's ratio
Hexagon based honeycombs	Regular hexagonal		$\frac{4}{\sqrt{3}}\left(\frac{t}{L}\right)^3$	1
	Hierarchical hexagonal		$\frac{4}{\sqrt{3}}\left(\frac{t}{L}\right)^3\left[\frac{1}{1-4.7(r/L)+4.8(r/L)^2+3.87(r/L)^3}\right]$	$1-\frac{(r/L)^3}{2.9(r/L)^3+3.6(r/L)^2-3.525(r/L)+0.75}$
	Tri-chiral		$\frac{4}{\sqrt{3}}\left(\frac{t}{L}\right)^3\left[\frac{3/2}{\cos^2(\pi/6-\theta)+4\sin^2\theta+\cos^2(\pi/6+\theta)}\right]$	$\sqrt{3}\left[\frac{\sin(\pi/6-\theta)\cos(\pi/6-\theta)+\sin(\pi/6+\theta)\cos(\pi/6+\theta)}{\cos^2(\pi/6-\theta)+4\sin^2\theta+\cos^2(\pi/6+\theta)}\right]$
	Anti-tri-chiral		$\frac{4}{\sqrt{3}}\left(\frac{t}{L}\right)^3\left[\frac{1}{1+24(r/L)^2}\right]$	$\frac{1-24(r/L)^2}{1+24(r/L)^2}$
Square based honeycombs	Square*		$\frac{t}{L}$	0
	Hierarchical square*		$\frac{t/L}{1-(r/L)+2.5(r/L)^3/(t/L)^2}$	$\frac{0.6(r/L)^3}{(r/L)^3-0.4(t/L)^2(r/L)+0.4(t/L)^2}$
	Hierarchical diamond*		$\frac{t/L}{1-(r/L)(2-1/\sqrt{2})+\sqrt{2}(r/L)^3/(t/L)^2}$	$\frac{(r/L)^3-0.5(t/L)^2(r/L)}{(r/L)^3-(\sqrt{2}-0.5)(t/L)^2(r/L)+(t/L)^2/\sqrt{2}}$
	Tetra-chiral*		$\frac{t/L}{\cos^2\theta+\sin^2\theta/(t/L)^2}$	0
	Anti-tetra-chiral*		$\frac{t/L}{1+6(r/L)^2/(t/L)^2}$	$\frac{-6(r/L)^2}{6(r/L)^2+(t/L)^2}$

Table 2
Summary of the analytical expressions for the effective shear modulus and material principal directions for the anisotropic lattices studied.

	Name	Unit cell	Effective shear modulus	Principal direction
Square based honeycombs	Square		$0.5\left(\frac{t}{L}\right)^3$	$\frac{k\pi}{4}$
	Hierarchical square		$\frac{0.5(t/L)^3}{1-3(r/L)-6(r/L)^2+20(r/L)^3+(t/L)^2(r/L)}$	$\frac{k\pi}{4}$
	Hierarchical diamond		$\frac{0.5(t/L)^3}{[1-2(r/L)]^2\left[1+(1.5\sqrt{2}-2)(r/L)\right]+\sqrt{2}(t/L)^2(r/L)}$	$\frac{k\pi}{4}$
	Tetra-chiral		$\frac{0.5(t/L)^3}{\cos^2\theta+(t/L)^2\sin^2\theta}$	$\frac{k\pi}{4}-\frac{\theta}{2}$
	Anti-tetra-chiral		$0.5\left(\frac{t}{L}\right)^3$	$\frac{k\pi}{4}$

is also the most compliant among the three exhibits auxeticity as Poisson's ratio becomes negative for r/R greater than $\cong$0.2.

Figure 8 illustrates the behavior of square based structures which are anisotropic. Since the results for stretching dominated honeycombs depend on the relative density of the structures, we reported the results of square based honeycombs only at a constant relative density of 6%. The solid lines in these figures represent the results from the closed-form estimates of elastic moduli from Tables 1 and 2, and markers denote the FE results. Similar to hexagon based honeycombs, there exist discrepancies between the theoretical and numerical results of square based structures in the case of chiral and anti-chiral lattices, which become more pronounced for tetra-chiral structure as r/R goes to 0.5. Again, these discrepancies stem from the assumed rigid behavior for the cylindrical components in the chiral and anti-chiral structures. We plot the normalized Young's modulus of the structure (effective Young's modulus of the structure normalized by the effective Young's modulus of a square honeycomb with same relative density) in Fig. 8(a) and notice a good agreement with FE results. Clearly, increasing r/R results in a sharp decrease in the in-plane stiffness of these structures which is especially pronounced in tetra- and anti-tetra-chiral lattices. Of all the square based structures studied, only anti-tetra-chiral honeycombs exhibit auxeticity for all values of r/R. In this structure, the Poisson's ratio starts to change quite appreciably with even small changes in r/R, then accelerates towards lesser values of r/R and finally reaches a plateau. On the other hand, although the tetra-chiral structure, along with the hierarchical structures show little initial sensitivity to the variations in r/R, at around $r/R \cong 0.03$, their behaviors begin to sharply diverge. The hierarchical structures show a rapid change followed by plateaus whereas the tetra-chiral structure starts with a slower variation which accelerates sharply as $r/R \rightarrow 0.5$ due to the effect of compliance of the cylinders as mentioned above. Finally Fig. 8(c) plots the variation of normalized shear

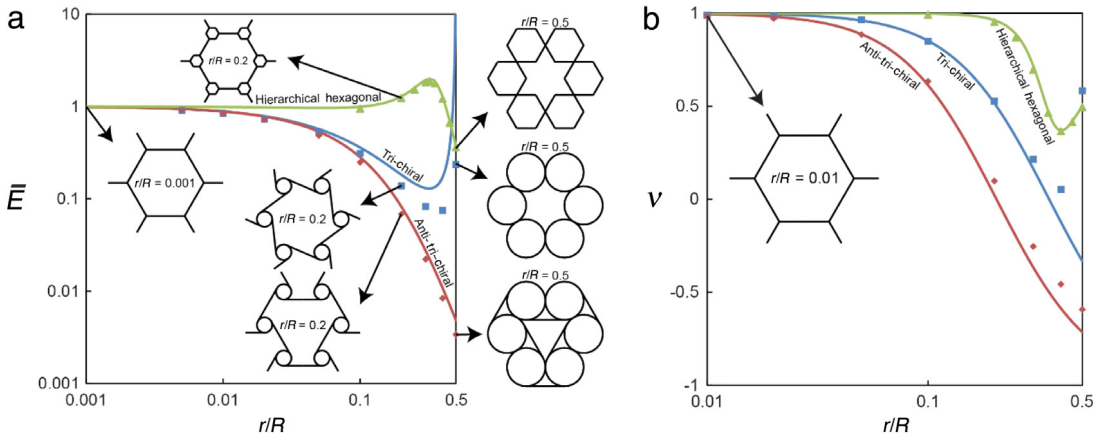

Fig. 7. (a) Normalized Young's modulus, and (b) Poisson ratio as a function of geometrical parameter, r/R, for three different hexagon based hierarchical and chiral lattices. The effective Young's modulus of the structure is normalized by the effective Young's modulus of a regular hexagonal honeycomb ($r/R = 0$) with same relative density. The solid lines represent the results from the theoretical estimates (i.e. relations reported in Table 1), and circles show the FE results.

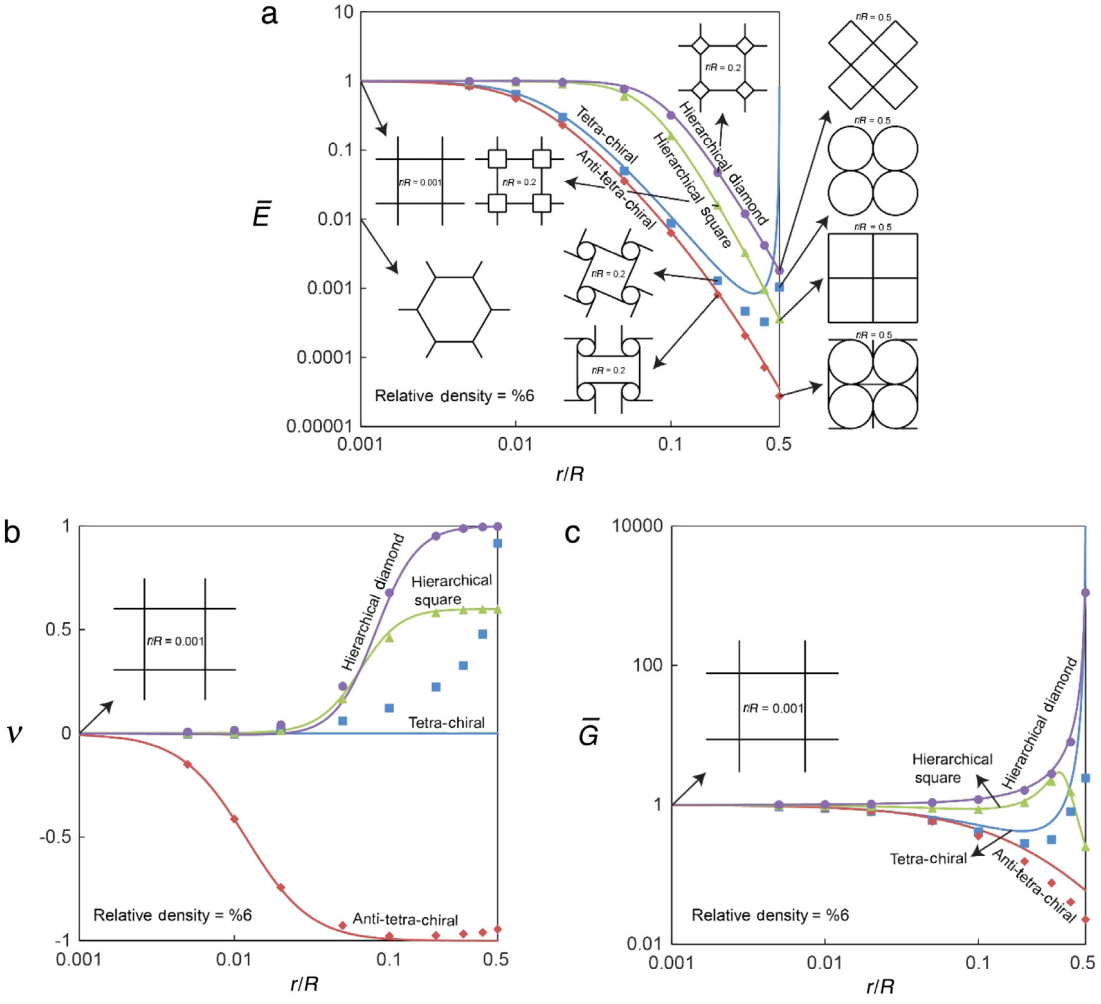

Fig. 8. (a) Normalized Young's modulus, (b) Poisson ratio, and (c) Normalized shear modulus as a function of geometrical parameter, r/R, for four different anisotropic square based hierarchical and chiral lattices. The effective Young's and shear moduli of the structure are normalized by those of a square honeycomb ($r/R = 0$) with same relative density. The solid lines represent the results from the theoretical estimates (i.e. relations reported in Tables 1 and 2), and circles show the FE results.

modulus (effective shear modulus of the structure normalized by the effective shear modulus of a square honeycomb with same relative density) of these anisotropic structures. The normalized shear moduli of the two chiral and two hierarchical structures show little initial sensitivity to variation of r/R. However, soon at about $r/R \cong 0.01$, these two groups diverge completely in opposite directions unlike previous elastic constants. The chiral structures show increasingly low normalized shear modulus as r/R is increased whereas an increase in r/R positively affects the normalized shear modulus of the hierarchical structures. The trend

Table 3
Our theoretical and numerical results vs. numerical and experimental data available in Ref. [46].

	Young's modulus (MPa)				Poisson's ratio			
Name	Theory	FE	FE [46]	EXP [46]	Theory	FE	FE [46]	EXP [46]
Tri-chiral	0.63	0.48	0.65	1.10	+0.57	+0.57	+0.60	+0.68
Anti-tri-chiral	0.41	0.34	0.39	0.61	+0.02	+0.11	+0.06	+0.08
Tetra-chiral	2.45	1.64	12.01	7.08	0.00	+0.20	−0.83	−0.26
Anti-tetra-chiral	1.42	1.32	2.50	3.11	−0.99	−0.96	−0.98	−0.98

for tetra-chiral structure changes course at an r/R of about 0.25 as the structure becomes increasingly stiff in shear, causing a rapid increase as $r/R \to 0.5$.

Next, we compare our results with numerical and experimental data available in the literature. We choose the reported data from Ref. [46] who carried out numerical and experimental analysis on the in-plane elastic properties of chiral and anti-chiral honeycombs subjected to uniaxial loading for small deformations. They employed selective laser sintering rapid-prototyping technique to fabricate the experimental samples out of nylon powder with geometrical parameters $r = 5$ mm, $L = 25$ mm, $t = 1.5$ mm, and out-of-plane depth $d = 25$ mm. Table 3 compares our results with their numerical and experimental data. From this table we find favorable comparisons of our elastic constants (Young's modulus and Poisson's ratio) for almost all chirality except the tetra-chiral case. Note that some discrepancy is natural both due to the difference in the materials between the two cases and also from the different boundary conditions employed between the two FE models. Specifically, in contrast to our periodic boundary conditions imposed on the FE models at structural level, they employed slightly different non-periodic boundary conditions at the "RVE level" which led to a stiffening effect on the RVEs. For instance, for tri- and anti-tri-chiral honeycombs, instead of applying appropriate forces and moments on the RVE's edge nodes to simulate the uniaxial loading on a periodic structure, they used geometrical constraints (i.e., coupling interaction between RVE's edge nodes) to relate the displacements of particular edge nodes within the RVE. We believe that this difference may play an even greater role in the relatively large discrepancy between the results obtained for the case of tetra-chiral honeycombs. Interestingly, for this particular case, Alderson et al. [46] report auxeticity for this structure at small strains through both FE and experimental investigations (Table 3) whereas neither our theoretical prediction, nor FE simulations as seen in Fig. 6 show any auxeticity for this case.

We studied the effects of chirality and hierarchy, generally a hallmark of natural materials, on the static in-plane properties of a selected set of 2D honeycombs. Analytical closed-form formulas for square and hexagon based networks have been obtained, and the results are verified numerically. Comprehensive design graphs, comparing elastic moduli (Young's and shear moduli and Poisson's ratio) are provided. We find that both chirality and hierarchy crucially affect the in-plane mechanical properties of these structures. Overall, hierarchical structures are stiffer and have higher Poisson's ratio than their chiral counterparts for similar values of the r/R ratio which quantifies the amount of hierarchy or chirality. However, chirality remains the only route to auxeticity. This is due to the deformation mechanism observed in auxetic chiral and anti-chiral honeycombs. This mechanism is characterized by the rotation of cylindrical nodes and bending of the ligaments, which make the structures contract in the transverse direction when subjected to uniaxial compressive loads. The behavior of the elastic constants of anti-tetra-chiral structure shows a remarkable glimpse of an engineered material which can simultaneously exhibit anisotropy, auxeticity, and a shear modulus that is much lower than usual solids.

Acknowledgments

The authors thank Dr. Jim Papadopoulos for many fruitful discussions. This report was made possible by a NPRP award (NPRP 7-882-2-326) from the Qatar National Research Fund (a member of the Qatar Foundation). The statements herein are solely the responsibility of the authors.

Appendix A. Tri-chiral

A schematic of a tri-chiral honeycomb derived from a regular hexagonal architecture undergoing an in-plane uniaxial far-field (macroscopic) loading in the x-direction characterized by the normal stress, σ_x is shown in Fig. A.1(a). A detailed FBD of the structural unit cell of this honeycomb is shown is Fig. A.1(b). The unit cell contains a cylinder (node) which is assumed to be rigid and three half ligaments. Due to the 180° rotational symmetry of the structure and the components of the microscopic stresses, all three external cut points of the unit cell (i.e., points 1 through 3 in Fig. A.1(b)) must be moment-free under an arbitrary macroscopic stress state. Therefore, utilizing the equilibrium conditions of forces and moments, the horizontal force, F, can be related to the far-field stress as, $F = \sigma_x R\sqrt{3}/2$, where R is the center to center distance of adjacent cylinders in the structure, as shown in Fig. A.1(b). The vertical force, P is a virtual force which will be used later in this subsection to compute the Poisson's ratio of the structure. Under the influence of this force system, neglecting the stretching and shearing terms, the strain energy stored in the unit cell of this bending dominated structure can be obtained as:

$$U = 1/(2E_sI)\left\{\int_0^{L/2}\left[(F\cos(\pi/6+\theta) - P\sin(\pi/6+\theta))\,x\right]^2 dx + \int_0^{L/2}\left[(2F\sin\theta)\,x\right]^2 dx + \int_0^{L/2}\left[(F\cos(\pi/6-\theta) - P\sin[\pi/6-\theta])\,x\right]^2 dx\right\}, \tag{A.1}$$

where E_s (as mentioned earlier) is the Young's modulus of the cell wall material, I is the second moment of area of the wall's cross section (cell walls are assumed to have a rectangular cross section with uniform thickness, t, and unit depth, i.e., $I = t^3/12$), and $\theta = \tan^{-1}(2r/L)$ is the angle between each ligament and the line connecting the centers of two adjacent cylinders as shown in Fig. A.1(b). Setting $P = 0$ in Eq. (A.1) and using Castigliano's second theorem [72], $\partial U/\partial F$ gives the total displacement (δ_x) of points 1 and 2 (with respect to point 3) in the x-direction. Then the average strain of the structure in the x-direction is obtained by using the relation, $\epsilon_x = \delta_x/(1.5R)$. The effective Young's modulus of the structure (normalized by material's Young's modulus, E_s) is then defined as the ratio of the average stress, σ_x, and the average strain, ϵ_x, and obtained as:

$$E/E_s = 4/\sqrt{3}\,(t/L)^3\left[1.5/\left(\cos^2(\pi/6-\theta) + 4\sin^2\theta + \cos^2(\pi/6+\theta)\right)\right]. \tag{A.2}$$

Note that as r goes to zero, θ also approaches zero and the structure is reduced to a regular hexagonal honeycomb. Thus, letting $\theta = 0$

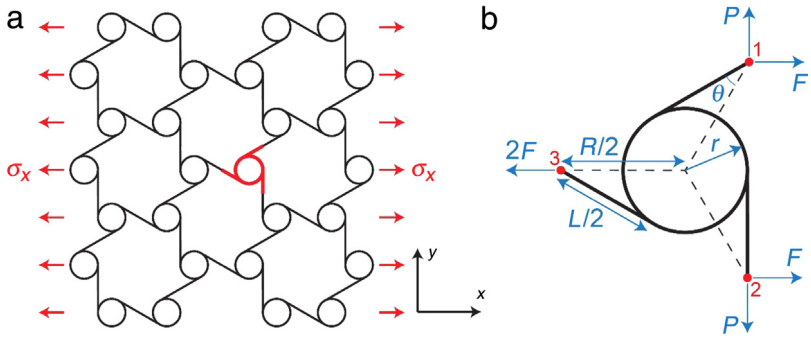

Fig. A.1. (a) Schematic of a tri-chiral honeycomb under x-direction uniaxial loading. (b) FBD of the structural unit cell.

in Eq. (A.2) will result in $E/E_s = 4/\sqrt{3}\,(t/L)^3$, which is a familiar result for the effective Young's modulus of a regular hexagonal honeycomb [75].

Next, to completely characterize the elastic behavior of tri-chiral honeycomb, we also need to determine its Poisson's ratio, ν. We again used Castigliano's second theorem to obtain the displacement between points 1 and 2 (δ_y) (see Fig. A.1(b)) in the direction of the virtual forces as, $\delta_y = \partial U/\partial P|_{P=0}$. Using this relation we obtain $\epsilon_y = \delta_y/\left(R\sqrt{3}/2\right)$ which gives the structure's average strain in the y-direction due to the uniaxial loading, σ_x in the x-direction. The effective Poisson's ratio, ν, of the structure is finally defined as the negative of the ratio of the average strain in the y-direction, ϵ_y, to the average strain in the x-direction, ϵ_x, and obtained as the following:

$$\nu = \sqrt{3}\frac{[\sin(\pi/6-\theta)\cos(\pi/6-\theta)+\sin(\pi/6+\theta)\cos(\pi/6+\theta)]}{\cos^2(\pi/6-\theta)+4\sin^2\theta+\cos^2(\pi/6+\theta)}. \tag{A.3}$$

Again, note that as r goes to zero, Eq. (A.3) reduces to $\nu = 1$, which is the effective Poisson's ratio of a regular hexagonal honeycomb [75].

Appendix B. Anti-tri-chiral

A schematic of an anti-tri-chiral structure which is also derived from an underlying hexagonal unit cell architecture is shown in Fig. B.1(a). An in-plane uniaxial far-field loading characterized by the normal stress, σ_x is applied to the structure in the x-direction. A detailed FBD of the structural unit cell is also shown in Fig. B.1(b). It contains a rigid cylinder (node) and three half ligaments. As shown in Fig. B.1(a), by using a cut line Δ_1, since there is no macroscopic stress to the structure in the y-direction, the unit cell must be free of any forces in the y-direction at point 1. Similar argument holds true for point 2 (by using the cut line Δ_2 in Fig. B.1(a)). Furthermore, due to the symmetry of the structure with respect to the cut line Δ_3 (see Fig. B.1(a)), point 3 must also be free of any forces in the y-direction. Then, using the zigzag cut line Δ_4 shown in Fig. B.1(a) and due to the symmetry of the structure mentioned above; points 1 and 2 must experience same forces in the x-direction and same moments with respect to the z-axis. Thus, the forces and moments acting on the external cut points of the unit cell are reduced as shown in Fig. B.1(b) (recall from previous section that the virtual force P has been applied to calculate the Poisson's ratio and can be treated as zero in this part of the calculation). Note that the x-component of the force applied to point 3 (i.e., $2F$) comes from the equilibrium of forces in the x-direction. Now, the equilibrium of moments in the z-direction gives $2M + M^* - 3rF = 0$, where M and M^* are two yet unknown moments at external cut points of the unit cell as a result of the loading on the structure. Using this equation and neglecting the stretching and shearing terms, the strain energy stored in the unit cell is obtained as:

$$U = 1/(2E_sI)\left[\int_0^{L/2}(2M-3rF)^2\mathrm{d}x + \int_0^{L/2}(M+Fx\sqrt{3}/2)^2\mathrm{d}x + \int_0^{L/2}(M-Fx\sqrt{3}/2)^2\mathrm{d}x\right]. \tag{B.1}$$

Now, for all horizontal lines of the structure to remain parallel in the deformed state, we can show that the following geometrical condition must hold: $\theta_1 = -\theta_2$, where θ_1 and θ_2 are respectively the total rotations of points 1 and 2 with respect to the z-axis. Using Castigliano's theorem, this geometrical condition is equivalent to the relation, $\partial U/\partial M = 0$. Now, substituting into this equation the strain energy given by Eq. (B.1), M is determined as a function of F as $M = rF$. Also using equation of equilibrium for the moments given earlier, M^* is obtained as $M^* = rF$. Next, substituting the values obtained for unknown moments M and M^* into Eq. (B.1), the strain energy stored in the unit cell can be written as:

$$U = 1/(2E_sI)\left[\int_0^{L/2}(rF)^2\mathrm{d}x + \int_0^{L/2}(rF+Fx\sqrt{3}/2)^2\mathrm{d}x + \int_0^{L/2}(rF-Fx\sqrt{3}/2)^2\mathrm{d}x\right], \tag{B.2}$$

where F can be obtained as a function of the applying stress, σ_x as $F = L\sigma_x\sqrt{3}/2$.

Using Castigliano's second theorem, $\partial U/\partial F$ gives the total displacements of points 1 and 2 (with respect to point 3) in the loading direction as, $\delta_x = \frac{FL(L^2+24r^2)}{16E_sI}$. Furthermore, the structure's average strain in the x-direction is obtained by using the relation, $\epsilon_x = \delta_x/(1.5L)$. The effective Young's modulus of the structure (normalized by material's Young's modulus, E_s) is then defined as the ratio of the average stress, σ_x and the average strain, ϵ_x and obtained as:

$$E/E_s = 4/\sqrt{3}\,(t/L)^3/[1+24\,(r/L)^2]. \tag{B.3}$$

In the remaining part of this subsection, in order to obtain the Poisson's ratio of the structure we add two virtual forces, P acting on points 1 and 2 of the unit cell, as shown in Fig. B.1(b). Note that for the unit cell to remain in the static equilibrium state, we also need to add a virtual moment ($Pr\sqrt{3}$) with respect to the z-axis acting on point 3. Thus, the strain energy stored in the unit cell will be modified as follows:

$$U = 1/(2E_sI)\left[\int_0^{L/2}\left(rF+Pr\sqrt{3}\right)^2\mathrm{d}x + \int_0^{L/2}\left(rF+Fx\sqrt{3}/2-Px/2\right)^2\mathrm{d}x + \int_0^{L/2}\left(rF-Fx\sqrt{3}/2+Px/2\right)^2\mathrm{d}x\right]. \tag{B.4}$$

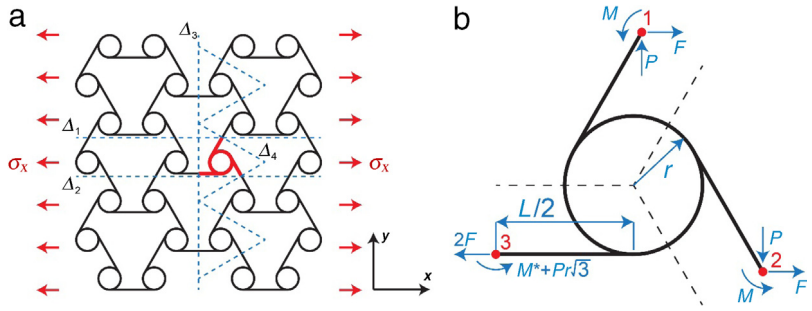

Fig. B.1. (a) Schematic of an anti-tri-chiral honeycomb under x-direction uniaxial loading. (b) FBD of the structural unit cell.

Next, we use Castigliano's second theorem to obtain the total displacement of points 1 and 2 (see Fig. B.1(b)) in the direction of the virtual forces as, $\delta_y = \partial U/\partial P|_{P=0}$. Using Eq. (B.4), δ_y is obtained as, $\delta_y = \frac{FL\sqrt{3}(24r^2-L^2)}{48E_sI}$. Then, using this equation, $\epsilon_y = \delta_y/\left(L\sqrt{3}/2\right)$ gives the structure's average strain in the y-direction due to the uniaxial loading in the x-direction (σ_x). The effective Poisson's ratio, ν of the structure is then defined as the negative of the ratio of the average strain in the y-direction, ϵ_y to the average strain in the x-direction, ϵ_x and given as follows:

$$\nu = \frac{1-24\,(r/L)^2}{1+24\,(r/L)^2}. \tag{B.5}$$

Note that similar to the tri-chiral structure, here as r goes to zero, the structure transforms into a regular hexagonal honeycomb. Letting $r = 0$ in Eqs. (B.3) and (B.5) will result in $E/E_s = 4/\sqrt{3}\,(t/L)^3$, and $\nu = 1$, which are the effective Young's modulus and Poisson's ratio of a regular hexagonal honeycomb, respectively, as noted earlier.

Appendix C. Anti-tetra-chiral

We now turn our attention to the next alteration of the square based unit cell which is an anti-tetra-chiral structure. Note that the Young's modulus and Poisson's ratio of the anti-tetra-chiral lattice with square and rectangle based networks have been analytically determined assuming the square based anti-tetra-chiral lattice (i.e., when all straight beams having identical lengths) is macroscopically isotropic [33]. In contrast, in the current paper we will show that the square anti-tetra-chiral structure is macroscopically orthotropic (i.e., having four-fold rotational symmetry and defined by three in-plane materials constants), and will derive analytical relations for the shear modulus and the material's principal directions.

An anti-tetra-chiral structure is depicted schematically in Fig. C.1(a) under a uniaxial far-field stress in the x-direction, σ_x. FBD of a representative unit cell of the structure is shown in Fig. C.1(b). It contains a rigid cylinder (node) and four half ligaments. The 180° rotational symmetry of the structure and loading, requires that any two external cut points (i.e., points 1 through 4 in Fig. C.1(b)) located opposite to each other in the unit cell experience same forces and moments. Then, using the cut line Δ_1, since there is no macroscopic stress applied to the structure in the y-direction, the unit cell must be forceless in that direction at point 4. Similar statement holds true for point 2, by using the cut line Δ_2. Also note that the component of forces parallel to each cut line at corresponding external cut point of the unit cell must be equal to zero, because no macroscopic shear stress acts on the structure. Thus, under this uniaxial stress on the structure, σ_x, each unit cell experiences the loading shown in Fig. C.1(b) (for instance neglect the terms containing P in the forces and moments), where F can be given as a function of applied stress as, $F = \sigma_x L$. Also, M and M^* are two yet unknown moments to be determined. Then, equilibrium of moments with respect to the z-axis gives $M + M^* - rF = 0$. Using this equation and neglecting the shearing terms, the strain energy of the unit cell can be written as, $U = 2\frac{F^2L/2}{2E_sA} + 2\int_0^{L/2}\frac{M^2}{2E_sI}\mathrm{d}x + 2\int_0^{L/2}\frac{(rF-M)^2}{2E_sI}\mathrm{d}x$. Next, for all horizontal lines in the structure to remain parallel in the deformed state, the following condition must hold: $\frac{\partial U}{\partial M} = 0$. Upon substituting the strain energy into this equation, M is obtained as a function of F as $M = rF/2$. Then, using the equation of equilibrium of moments given earlier, M^* is also obtained as $M^* = rF/2$. Then, substituting the values obtained for unknown moments, M and M^* into the equation of strain energy, it will be modified as $U = 2\frac{F^2L/2}{2E_sA} + 4\frac{(rF/2)^2L/2}{2E_sI}$. Using Castigliano's theorem, $\partial U/\partial F$ gives the total displacement of point 1 with respect to the point 3 in the x-direction as $\delta_x = \frac{FL}{E_sA} + \frac{Fr^2L}{2E_sI}$. Then the structure's average strain in the x-direction is given by using the relation, $\epsilon_x = \delta_x/L$. The effective Young's modulus of the structure (normalized by material's Young's modulus, E_s) is then defined as the ratio of the average stress, σ_x and the average strain, ϵ_x and obtained as:

$$E_x/E_s = \frac{t/L}{1+6\,(r/L)^2/\,(t/L)^2}. \tag{C.1}$$

Next, in order to obtain the Poisson's ratio of the structure, we add two virtual forces of magnitude P acting on points 2 and 4 as shown in Fig. C.1(b) to be able to find the elongation of the unit cell in the y-direction. Note that for the unit cell to remain in the equilibrium state, we must include virtual moments, $rP/2$, with respect to the z-axis acting on points 1 through 4 (see Fig. C.1(b)). Thus, the strain energy of the unit cell will be modified into: $U = 2\frac{F^2L/2}{2E_sA} + 2\frac{P^2L/2}{2E_sA} + 4\frac{(rF/2+rP/2)^2L/2}{2E_sI}$. Then, using Castigliano's theorem, the displacement of point 4 with respect to point 2 in the y-direction can be obtained as, $\delta_y = \frac{Fr^2L}{2E_sI}$. Using this equation, $\epsilon_y = \delta_y/L$ gives the structure's average strain in the y-direction due to the uniaxial loading, σ_x. The effective Poisson's ratio of the structure is then defined as the negative of the ratio of the average strain in the y-direction, ϵ_y to the average strain in the x-direction, ϵ_x and obtained as follows:

$$\nu_{xy} = \frac{-6\,(r/L)^2}{6\,(r/L)^2+(t/L)^2}. \tag{C.2}$$

Finally, to determine the shear modulus, as shown in Fig. C.1(c), consider an anti-tetra-chiral structure under a uniform far-field shear stress, τ_{xy}. A representative unit cell of the structure is also shown in Fig. C.1(d). Similar to tetra-chiral honeycombs studied in the paper, we can show that under the shearing load, τ_{xy}, the unit cell must experience the loading shown in Fig. C.1(d), where F can be obtained as a function of applying stress as, $F = \tau_{xy}L$. Thus, the unit cell's strain energy is obtained as $U = 4\int_0^{L/2}\frac{(Fx)^2}{2E_sI}\mathrm{d}x$.

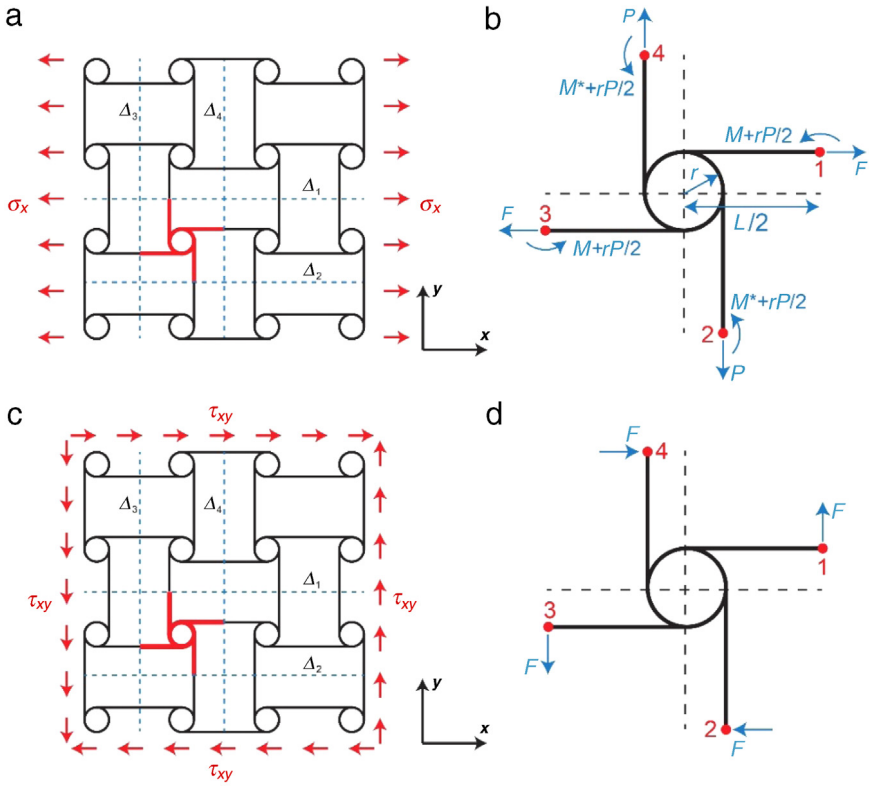

Fig. C.1. (a) Schematic of an anti-tetra-chiral honeycomb under x-direction uniaxial loading. (b) FBD of the structural unit cell under uniaxial loading. (c) Schematic of an anti-tetra-chiral honeycomb under x–y shearing load. (d) FBD of the structural unit cell under shearing load.

Then, $(\partial U/\partial F)/L$ gives the total change of angle (i.e., the shear strain, γ_{xy}) between two straight lines initially parallel to the x- and y-axes. Finally, the effective shear modulus of the structure (G_{xy}, normalized with respect to the Young's modulus of cell wall material) is defined as the ratio of the average shear stress, τ_{xy} to the average shear strain, γ_{xy} and obtained as the following:

$$G_{xy}/E_s = 0.5\,(t/L)^3\,. \tag{C.3}$$

Note that as r goes to zero, the structure transforms into a regular square honeycomb. Upon substituting $r = 0$ into Eqs. (C.1)–(C.3), we get $E_x/E_s = t/L$, $\nu_{xy} = 0$, and $G_{xy}/E_s = 0.5\,(t/L)^3$, which are the Young's modulus, Poisson's ratio, and shear modulus of a regular square honeycomb, respectively. Employing the same procedure as outlined in the paper yields the principal directions for the two-dimensional compliance tensor of this honeycomb as $k\pi/4$, where k is an integer.

Appendix D. Hierarchical diamond

We now turn our attention to determining the linear elastic constants of hierarchical diamond structure. Figure D.1(a) shows a hierarchical diamond structure under a uniaxial far-field stress in the x-direction, σ_x. The corresponding FBD of the unit cell is shown in Fig. D.1(b). It contains a diamond and four half ligaments connecting the diamonds together. Similar to the previous section, under a uniaxial stress on the structure, σ_x, each unit cell experiences the loading shown in Fig. D.1(b), where F can be obtained as a function of applied stress as, $F = \sigma_x L$. Consider the right portion of the unit cell as shown in Fig. D.1(b). Unknown forces and moment acting on points 5 and 6 of the unit cell are obtained by satisfying the equilibrium conditions discussed earlier. M is found to be $M = rF/4$. Then, using this equation, the unit cell's strain energy is obtained as:

$$U = 2\frac{F^2\,(L/2-r)}{2E_sA} + 4\frac{\left(F\sqrt{2}/4\right)^2 r\sqrt{2}}{2E_sA} + 4\int_0^{r\sqrt{2}} \frac{\left(rF/4 - xF\sqrt{2}/4\right)^2}{2E_sI}\mathrm{d}x. \tag{D.1}$$

Using above equation we can obtain the total displacement of point 1 with respect to point 3 in the x-direction as $\delta_x = \frac{\partial U}{\partial F} = \frac{F\left[L - r\left(2-1/\sqrt{2}\right)\right]}{E_sA} + \frac{\sqrt{2}Fr^3}{12E_sI}$. Next, the structure's average strain in the x-direction is obtained by using the relation $\epsilon_x = \delta_x/L$. The effective Young's modulus of the structure (normalized by material's Young's modulus, E_s) is then defined as the ratio of the average stress, σ_x and the average strain, ϵ_x and obtained as:

$$E_x/E_s = \frac{t/L}{1-(r/L)\left(2-1/\sqrt{2}\right) + \sqrt{2}\,(r/L)^3/(t/L)^2}. \tag{D.2}$$

Next, in order to obtain the Poisson's ratio, consider a pair of virtual forces acting on the unit cell in the lateral direction, as shown in Fig. D.1(c). One fourth of the diamond is also shown in Fig. D.1(c). Similar procedure is used to determine the unknown moments (M_1 and M_2) acting on points 6 and 7. M_1 and M_2 are obtained as $M_1 = -M_2 = rF/4 - rP/4$. Then, the strain energy of the unit cell is given as:

$$U = 2\frac{F^2\,(L/2-r)}{2E_sA} + 2\frac{P^2\,(L/2-r)}{2E_sA} + 4\frac{\left[(F+P)\sqrt{2}/4\right]^2 r\sqrt{2}}{2E_sA} + 4\int_0^{r\sqrt{2}} \frac{\left[\left(r/4 - x\sqrt{2}/4\right)(P-F)\right]^2}{2E_sI}\mathrm{d}x. \tag{D.3}$$

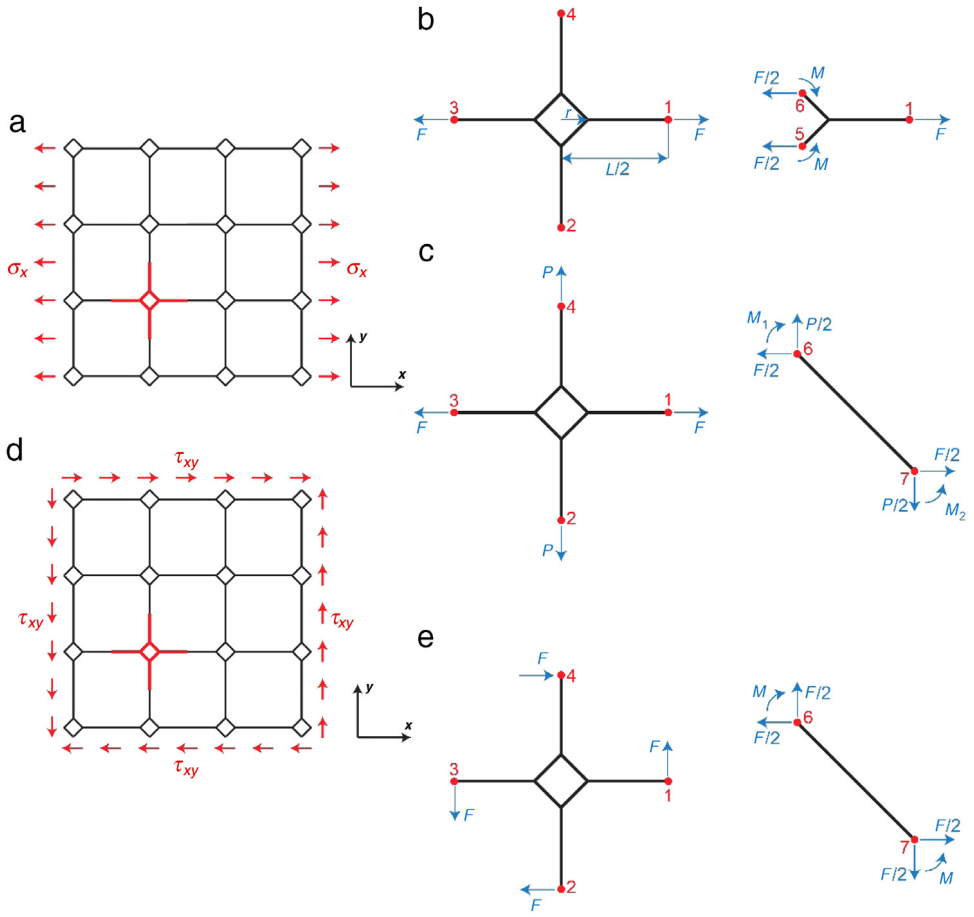

Fig. D.1. (a) Schematic of a hierarchical diamond honeycomb under x-direction uniaxial loading. (b) and (c) FBD of the structural unit cell under uniaxial loading, where P is a virtual force used for Poisson's ratio calculations. (d) Schematic of a hierarchical diamond honeycomb under x-y shearing load. (e) FBD of the structural unit cell under shearing load.

Castigliano's second theorem states that the total displacement of points 2 and 4 in the direction of virtual forces can be obtained using the relation, $\delta_y = \partial U/\partial P|_{P=0}$. Substituting Eq. (D.3) into this equation gives, $\delta_y = \frac{Fr}{\sqrt{2}E_sA} - \frac{\sqrt{2}Fr^3}{12E_sI}$. Then, using this equation, $\epsilon_y = \delta_y/L$ gives the structure's average strain in the y-direction due to the uniaxial loading, σ_x. The effective Poisson's ratio of the structure is then defined as the negative of the ratio of the average strain in the y-direction, ϵ_y to the average strain in the x-direction, ϵ_x and obtained as the following:

$$\nu_{xy} = \frac{(r/L)^3 - 0.5\,(t/L)^2\,(r/L)}{(r/L)^3 - \left(\sqrt{2} - 0.5\right)(t/L)^2\,(r/L) + (t/L)^2/\sqrt{2}}. \tag{D.4}$$

Finally, to determine the shear modulus, as shown in Fig. D.1(d), we apply a uniform far-field shear stress, τ_{xy} to a typical hierarchical diamond honeycomb. FBD of the unit cell is also shown in Fig. D.1(e). Likewise the previous section, there are only four equal shear forces acting on the unit cell's external cut points, F, which can be obtained as a function of applying stress as, $F = \tau_{xy}L$. Next, consider one fourth of the diamond as shown in Fig. D.1(e). Components of unknown forces and moment acting on the external cut points of this portion of the unit cell can be determined as functions of F, as shown in Fig. D.1(e), where $M = F/2\,(L/2 - r)$. Hence, the strain energy of the unit cell is obtained as:

$$U = 4\int_0^{L/2-r} \frac{(Fx)^2}{2E_sI}\mathrm{d}x + 4\frac{\left(F/\sqrt{2}\right)^2 r\sqrt{2}}{2E_sA} + 4\int_0^{r\sqrt{2}} \frac{[F/2\,(L/2 - r)]^2}{2E_sI}\mathrm{d}x. \tag{D.5}$$

Then, $(\partial U/\partial F)/L$ gives the total change of angle (i.e., the shear strain, γ_{xy}) between two straight lines initially parallel to the x- and y-axes. Finally, the effective shear modulus of the structure (G_{xy}, normalized with respect to the Young's modulus of cell walls material) is defined as the ratio of the average shear stress, τ_{xy} to the average shear strain, γ_{xy} and obtained as the following:

$$G_{xy}/E_s = \frac{0.5\,(t/L)^3}{[1 - 2\,(r/L)]^2\left[1 + \left(1.5\sqrt{2} - 2\right)(r/L)\right] + \sqrt{2}\,(t/L)^2\,(r/L)}. \tag{D.6}$$

Note that as r goes to zero, the structure transforms into a regular square honeycomb. Upon substituting $r = 0$ into Eqs. (D.2), (D.4) and (D.6), we get $E_x/E_s = t/L$, $\nu_{xy} = 0$, and $G_{xy}/E_s = 0.5\,(t/L)^3$, which are the Young's modulus, Poisson's ratio, and shear modulus of a regular square honeycomb, respectively. The principal directions for the two-dimensional compliance tensor of this structure are $\alpha = k\pi/4$, where k is an integer.

References

[1] S. Lubkin, Unidirectional waves on rings: Models for chiral preference of circumnutating plants, Bull. Math. Biol. 56 (1994) 795–810.
[2] M. Oliverio, M.C. Digilio, P. Versacci, et al., Shells and heart: Are human laterality and chirality of snails controlled by the same maternal genes? Am. J. Med. Genet. Part A 152A (2010) 2419–2425.

[3] M. Schilthuizen, A. Davison, The convoluted evolution of snail chirality, Naturwissenschaften 92 (2005) 504–515.
[4] R.R. Sinden, DNA Structure and Function, Gulf Professional Publishing, 1994.
[5] Z.L. Zhao, B. Li, X.Q. Feng, Hardedness-dependent hyperelasticity of biological soft fibers with multilayered helical structures, Int. J. Non-Linear Mech. 81 (2016) 19–29.
[6] J. Aizenberg, J.C. Weaver, M.S. Thanawala, et al., Skeleton of euplectella sp.: Structural hierarchy from the nanoscale to the macroscale, Science 309 (2005) 275–278.
[7] M.J. Buehler, Nature designs tough collagen: Explaining the nanostructure of collagen fibrils, Proc. Natl. Acad. Sci. 103 (2006) 12285–12290.
[8] H.D. Espinosa, A.L. Juster, F.J. Latourte, et al., Tablet-level origin of toughening in abalone shells and translation to synthetic composite materials, Nature Commun. 2 (2011) 173.
[9] P. Fratzl, R. Weinkamer, Nature's hierarchical materials, Prog. Mater. Sci. 52 (2007) 1263–1334.
[10] L.J. Gibson, M.F. Ashby, B.A. Harley, Cellular Materials in Nature and Medicine, Cambridge University Press, 2010.
[11] R. Lakes, Materials with structural hierarchy, Nature 361 (1993) 511–515.
[12] C. Ortiz, M.C. Boyce, Bioinspired structural materials, Science 319 (2008) 1053–1054.
[13] H. Qing, L. Mishnaevsky Jr., 3D hierarchical computational model of wood as a cellular material with fibril reinforced, heterogeneous multiple layers, Mech. Mater. 41 (2009) 1034–1049.
[14] J.S. Wang, G. Wang, X.Q. Feng, et al., Hierarchical chirality transfer in the growth of Towel Gourd tendrils, Sci. Rep. 3 (2013) 03102.
[15] Z.L. Zhao, H.P. Zhao, J.S. Wang, et al., Mechanical properties of carbon nanotube ropes with hierarchical helical structures, J. Mech. Phys. Solids 71 (2014) 64–83.
[16] N. Fang, D. Xi, J. Xu, et al., Ultrasonic metamaterials with negative modulus, Nat. Mater. 5 (2006) 452–456.
[17] Z. Liu, X. Zhang, Y. Mao, et al., Locally resonant sonic materials, Science 289 (2000) 1734–1736.
[18] R. Lakes, T. Lee, A. Bersie, et al., Extreme damping in composite materials with negative-stiffness inclusions, Nature 410 (2001) 565–567.
[19] U.D. Larsen, O. Sigmund, S. Bouwstra, Design and fabrication of compliant micromechanisms and structures with negative Poisson's ratio, in: Micro Electro Mechanical Systems, MEMS'96, Proceedings, An Investigation of Micro Structures, Sensors, Actuators, Machines and Systems, IEEE, The Ninth Annual International Workshop on, IEEE, 1996, pp. 365–371.
[20] R. Lakes, Foam structures with a negative Poisson's ratio, Science 235 (1987) 1038–1040.
[21] E. Friis, R. Lakes, J. Park, Negative Poisson's ratio polymeric and metallic foams, J. Mater. Sci. 23 (1988) 4406–4414.
[22] C. Körner, Y. Liebold-Ribeiro, A systematic approach to identify cellular auxetic materials, Smart Mater. Struct. 24 (2015) 025013.
[23] O. Sigmund, S. Torquato, Design of materials with extreme thermal expansion using a three-phase topology optimization method, J. Mech. Phys. Solids 45 (1997) 1037–1067.
[24] C.A. Steeves, S.L. Dos Santos E Lucato, M. He, et al., Concepts for structurally robust materials that combine low thermal expansion with high stiffness, J. Mech. Phys. Solids 55 (2007) 1803–1822.
[25] O. Sigmund, S. Torquato, Composites with extremal thermal expansion coefficients, Appl. Phys. Lett. 69 (1996) 3203–3205.
[26] F. Scarpa, Auxetic materials for bioprostheses [In the Spotlight], IEEE Signal Process. Mag. 25 (2008) 126–128.
[27] J. Choi, R. Lakes, Design of a fastener based on negative Poisson's ratio foam, Cell. Polymers 10 (1991) 205–212.
[28] O. Sigmund, S. Torquato, I.A. Aksay, On the design of 1–3 piezocomposites using topology optimization, J. Mater. Res. 13 (1998) 1038–1048.
[29] K. Evans, K. Alderson, Auxetic materials: the positive side of being negative, Eng. Sci. Educ. J 9 (2000) 148–154.
[30] F. Scarpa, G. Burriesci, F. Smith, et al., Mechanical and electromagnetic behaviour of auxetic honeycomb structures, Aeronaut. J. 107 (2003) 175.
[31] F. Scarpa, L. Ciffo, J. Yates, Dynamic properties of high structural integrity auxetic open cell foam, Smart Mater. Struct. 13 (2004) 49.
[32] A. Spadoni, M. Ruzzene, Elasto-static micropolar behavior of a chiral auxetic lattice, J. Mech. Phys. Solids 60 (2012) 156–171.
[33] Y. Chen, F. Scarpa, Y. Liu, et al., Elasticity of anti-tetrachiral anisotropic lattices, Int. J. Solids Struct. 50 (2013) 996–1004.
[34] O. Levy, S. Krylov, I. Goldfarb, Design considerations for negative Poisson ratio structures under large deflection for MEMS applications, Smart Mater. Struct. 15 (2006) 1459.
[35] R.J. Jackman, S.T. Brittain, A. Adams, et al., Design and fabrication of topologically complex, three-dimensional microstructures, Science 280 (1998) 2089–2091.
[36] G. Lesieutre, J.A. Browne, M. Frecker, Scaling of performance, weight, and actuation of a 2-D compliant cellular frame structure for a morphing wing, J. Intell. Mater. Syst. Struct. 22 (2011) 979–986.
[37] K.R. Olympio, F. Gandhi, Flexible skins for morphing aircraft using cellular honeycomb cores, J. Intell. Mater. Syst. Struct. 21 (2010) 1719–1735.
[38] E.A. Bubert, B.K. Woods, K. Lee, et al., Design and fabrication of a passive 1D morphing aircraft skin, J. Intell. Mater. Syst. Struct. 21 (2010) 1699–1717.
[39] A. Spadoni, M. Ruzzene, Static aeroelastic response of chiral-core airfoils, J. Intell. Mater. Syst. Struct. 18 (2007) 1067–1075.
[40] H. Heo, J. Ju, D.-M. Kim, et al., Passive morphing airfoil with honeycombs, in: Proceedings of the ASME International Mechanical Engineering Congress and Exposition, IMECE2011-64350, Denver, CO, 2011.
[41] T. Johnson, M. Frecker, M. Abdalla, et al., Nonlinear analysis and optimization of diamond cell morphing wings, J. Intell. Mater. Syst. Struct. 20 (2009) 815–824.
[42] D. Bornengo, F. Scarpa, C. Remillat, Evaluation of hexagonal chiral structure for morphing airfoil concept, Proc. Inst. Mech. Eng. G 219 (2005) 185–192.
[43] J.L. Reed Jr., C.D. Hemmelgarn, B.M. Pelley, et al., Adaptive wing structures, in: Proc. of SPIE Vol, 2005, pp. 133.
[44] J. Ju, D.-M. Kim, K. Kim, Flexible cellular solid spokes of a non-pneumatic tire, Compos. Struct. 94 (2012) 2285–2295.
[45] J. Ju, B. Ananthasayanam, J.D. Summers, P. Joseph, Design of cellular shear bands of a non-pneumatic tire-investigation of contact pressure, SAE Int. J. Passenger Cars Mech. Syst. 3 (2010) 598–606.
[46] A. Alderson, K. Alderson, D. Attard, et al., Elastic constants of 3-, 4-and 6-connected chiral and anti-chiral honeycombs subject to uniaxial in-plane loading, Compos. Sci. Technol. 70 (2010) 1042–1048.
[47] A. Alderson, K.L. Alderson, G. Chirima, et al., The in-plane linear elastic constants and out-of-plane bending of 3-coordinated ligament and cylinder-ligament honeycombs, Compos. Sci. Technol. 70 (2010) 1034–1041.
[48] D. Prall, R. Lakes, Properties of a chiral honeycomb with a Poisson's ratio of—1, Int. J. Mech. Sci 39 (1997) 305–314.
[49] Y. Chen, X. Liu, G. Hu, et al., Micropolar continuum modelling of bi-dimensional tetrachiral lattices, Proc. R. Soc. A 470 (2014) 20130734.
[50] Y. Chen, X. Liu, G. Hu, Micropolar modeling of planar orthotropic rectangular chiral lattices, Comptes Rendus Mécanique 342 (2014) 273–283.
[51] A. Bacigalupo, L. Gambarotta, Homogenization of periodic hexa-and tetrachiral cellular solids, Compos. Struct. 116 (2014) 461–476.
[52] A. Ajdari, B.H. Jahromi, J. Papadopoulos, et al., Hierarchical honeycombs with tailorable properties, Int. J. Solids Struct. 49 (2012) 1413–1419.
[53] R. Oftadeh, B. Haghpanah, J. Papadopoulos, et al., Mechanics of anisotropic hierarchical honeycombs, Int. J. Mech. Sci. 81 (2014) 126–136.
[54] R. Oftadeh, B. Haghpanah, D. Vella, et al., Optimal fractal-like hierarchical honeycombs, Phys. Rev. Lett. 113 (2014) 104301.
[55] F. Barthelat, H. Espinosa, An experimental investigation of deformation and fracture of nacre–mother of pearl, Exp. Mech. 47 (2007) 311–324.
[56] N.M. Pugno, Mimicking nacre with super-nanotubes for producing optimized super-composites, Nanotechnology 17 (2006) 5480.
[57] Z. Zhang, Y.-W. Zhang, H. Gao, On optimal hierarchy of load-bearing biological materials, Proc. R. Soc. Lond. Biol. 278 (2011) 519–525.
[58] D. Mousanezhad, H. Ebrahimi, B. Haghpanah, et al., Spiderweb honeycombs, Int. J. Solids Struct. 66 (2015) 218–227.
[59] D. Rayneau-Kirkhope, Y. Mao, R. Farr, Ultralight fractal structures from hollow tubes, Phys. Rev. Lett. 109 (2012) 204301.
[60] B. Haghpanah, J. Papadopoulos, A. Vaziri, Plastic collapse of lattice structures under a general stress state, Mech. Mater. 68 (2014) 267–274.
[61] B. Haghpanah, J. Papadopoulos, D. Mousanezhad, et al., Buckling of regular, chiral and hierarchical honeycombs under a general macroscopic stress state, Proc. R. Soc. A 470 (2014) 20130856.
[62] Y. Sun, N. Pugno, Hierarchical fibers with a negative Poisson's ratio for tougher composites, Materials 6 (2013) 699–712.
[63] F. Song, J. Zhou, X. Xu, et al., Effect of a negative Poisson ratio in the tension of ceramics, Phys. Rev. Lett. 100 (2008) 245502.
[64] R. Lakes, High damping composite materials: effect of structural hierarchy, J. Compos. Mater. 36 (2002) 287–297.
[65] D. Mousanezhad, S. Babaee, H. Ebrahimi, et al., Hierarchical honeycomb auxetic metamaterials, Sci. Rep. 5 (2015) 18306.
[66] D. Mousanezhad, S. Babaee, R. Ghosh, et al., Honeycomb phononic crystals with self-similar hierarchy, Phys. Rev. B 92 (2015) 104304.
[67] R.S. Farr, Fractal design for an efficient shell strut under gentle compressive loading, Phys. Rev. E 76 (2007) 056608.
[68] R.S. Farr, Fractal design for efficient brittle plates under gentle pressure loading, Phys. Rev. E 76 (2007) 046601.
[69] D. Rayneau-Kirkhope, R. Farr, Y. Mao, Fractal-like dependence in the designs of efficient pressure-bearing structures, Europhys. Lett. 93 (2011) 34002.
[70] D. Rayneau-Kirkhope, Y. Mao, R. Farr, et al., Hierarchical space frames for high mechanical efficiency: Fabrication and mechanical testing, Mech. Res. Commun. 46 (2012) 41–46.
[71] B. Haghpanah, R. Oftadeh, J. Papadopoulos, et al., Self-similar hierarchical honeycombs, Proc. R. Soc. A 469 (2013) 20130022.
[72] A.P. Boresi, R.J. Schmidt, Advanced Mechanics of Materials, Wiley, 2003.
[73] R. Christensen, Sufficient symmetry conditions for isotropy of the elastic moduli tensor, J. Appl. Mech. 54 (1987) 772.
[74] L.J. Gibson, M.F. Ashby, Cellular Solids: Structure and Properties, Cambridge Univ. Pr., 1999.
[75] C.T. Herakovich, Mechanics of Fibrous Composites, first ed., Wiley, 1997.
[76] H. Harders, K. Hupfer, J. Rösler, Influence of cell wall shape and density on the mechanical behaviour of 2D foam structures, Acta Mater. 53 (2005) 1335–1345.